NIST Internal Report
NIST IR 8608

Alternative Fundamental Equation of State for Fluid Carbon Dioxide

Eric W. Lemmon
Allan H. Harvey
Robert Hellmann

This publication is available free of charge from:
https://doi.org/10.6028/NIST.IR.8608

NATIONAL INSTITUTE OF STANDARDS AND TECHNOLOGY
U.S. DEPARTMENT OF COMMERCE

NIST Internal Report
NIST IR 8608

Alternative Fundamental Equation of State for Fluid Carbon Dioxide

Eric W. Lemmon
Allan H. Harvey
Applied Chemicals and Materials Division
Material Measurement Laboratory

Robert Hellmann
Institut für Thermodynamik
Helmut-Schmidt-Universität / Universität der Bundeswehr Hamburg, Hamburg, Germany

This publication is available free of charge from:
https://doi.org/10.6028/NIST.IR.8608

February 2026

U.S. Department of Commerce
Howard Lutnick, Secretary

National Institute of Standards and Technology
Craig Burkhardt, Acting Under Secretary of Commerce for Standards and Technology and Acting NIST Director

Certain equipment, instruments, software, or materials, commercial or non-commercial, are identified in this paper in order to specify the experimental procedure adequately. Such identification does not imply recommendation or endorsement of any product or service by NIST, nor does it imply that the materials or equipment identified are necessarily the best available for the purpose.

Publication History
Approved by the NIST Editorial Review Board on 2026-01-29

How to cite this NIST Technical Series Publication:
Lemmon EW, Harvey AH, Hellmann R (2026) Alternative Fundamental Equation of State for Fluid Carbon Dioxide. (National Institute of Standards and Technology, Gaithersburg, MD), NIST Interagency or Internal Report (IR) NIST IR 8608. https://doi.org/10.6028/NIST.IR.8608

Author ORCID iDs
Eric W. Lemmon: 0000-0002-0974-0203
Allan H. Harvey: 0000-0002-0072-2332
Robert Hellmann: 0000-0003-3121-6827

Contact Information
allan.harvey@nist.gov

Abstract

We present a new fundamental equation of state for fluid carbon dioxide, which is an alternative to the current reference formulation published by Span and Wagner in 1996. The equation of state is formulated as the Helmholtz energy as a function of temperature and density. The ideal-gas term is based on new, high-accuracy results for the ideal-gas heat capacity. The real-gas term is fitted to a variety of critically assessed data sources, including several that were not available in 1996. The range of validity extends to 2000 K and 1000 MPa. The new equation of state performs similarly to that of Span and Wagner for most properties at most conditions, but is an improvement for virial coefficients and supercritical densities. It is also free of some minor unphysical behavior near the critical point exhibited by the Span–Wagner equation of state. The more efficient structure makes it faster than the Span–Wagner equation of state by a factor of 1.5–2 when implemented in NIST's REFPROP software.

New auxiliary equations are presented for the melting and sublimation curves. The previously published formulations for the viscosity and thermal conductivity of CO_2 were tested with the new equation of state; it was found that use of the new equation did not affect their accuracy so they can continue to be used with the same parameters.

Keywords

carbon dioxide; density; equation of state; heat capacity; sound speed; thermodynamic properties; virial coefficients.

Table of Contents

List of Tables

List of Figures

Acknowledgments

This work was supported by the U.S. Department of Energy, National Energy Technology Laboratory, under Interagency Agreement DE-FE0028668.

The early stages of the project benefited from data files supplied by Theresa Wiens, Monika Thol, and Roland Span, who also contributed to discussions about the project. Roland Span read an early draft of this report and had several useful suggestions.

Several researchers kindly provided useful data that did not appear (or only appeared graphically) in their publications. We particularly thank Joe Magee, who delved into old computer files to supply necessary information related to his 1986 work, and Jan Sengers who supplied a similarly old paper copy of the data corresponding to the 1987 paper of Albright et al. We also thank Evan Abramson (who sadly did not live to see this use of his data), Frédéric Datchi (who also gave guidance on use of the Brillouin scattering data from his group), and Aliye Kartal Dogan for supplying unpublished data points. We thank Martin Trusler for helpful suggestions regarding data sources, Ilmutdin Abdualgatov for sharing additional details about his work and other work conducted in Dagestan, Patrick Rourke for insight concerning the 1992 publication of Ancsin, Susanne Picard for supplying a copy of a 1978 CCT report, Norbert Kurzeja for supplying results of Ref. 22 in digital form and for clarifications concerning that paper, Yvonne Leusmann for assistance with German literature, Ala Bazyleva and Ilmutdin Abdulagatov for assistance with Russian literature, and Boris Wilthan for digitizing some graphical data.

We also thank Marcia Huber of NIST for performing the validation of transport property correlations reported in Sec. 11.

1. Introduction

Accurate thermophysical properties of carbon dioxide (CO_2) are important for design and optimization in several contexts, particularly those related to power generation. Some proposed advanced power cycles can incorporate carbon capture within the cycle itself rather than removing CO_2 from the flue gas [1, 2]. A growing area of interest is the use of supercritical CO_2 as a working fluid in power cycles, either as an alternative to water/steam in a closed cycle or in the context of a combustion turbine that produces CO_2-rich gas. The use of carbon dioxide as the working fluid can produce efficiency advantages compared to steam; it can also allow more compact turbines and reduce the materials problems that can arise with hot H_2O [3–5].

In all of these contexts, design and modeling requires an accurate and well-behaved equation of state (EOS) for carbon dioxide [6–8]. This is obviously true for applications where the CO_2 is nearly pure, such as pipeline transport or use of supercritical CO_2 as a working fluid. However, the carbon dioxide EOS is equally important for mixtures—both in the obvious sense of providing an accurate contribution to the mixture properties but also because its numerical behavior, including in extrapolation regions, can produce problems in mixture calculations.

Currently, the standard source for CO_2 thermodynamic properties, both for pure CO_2 and within mixtures, is the reference-quality equation of state published by Span and Wagner in 1996 [9]. This is implemented in standard thermodynamic property packages such as NIST's REFPROP program [10]. The Span–Wagner EOS is valid at temperatures to 1100 K and pressures to 800 MPa; while this encompasses the range of expected power-cycle applications, the experimental basis for the EOS is rather sparse above about 700 K.

While it is adequate for most purposes, some shortcomings have been identified in the Span–Wagner EOS. There is more uncertainty than desired at high temperatures, and in general the extrapolation behavior (both to high and low temperatures) is not as good as can be obtained with modern EOS technology. The extrapolation issues can cause problems when CO_2 is used in mixture calculations. There is also unphysical behavior in some derivative properties near the critical point, which among other things causes unphysical behavior in the thermal conductivity in this region [11]. The form of the EOS is rather complex, making it computationally slower than desired for some applications. Finally, new experimental and theoretical information that can improve the accuracy of the EOS has been obtained since 1996.

In this work, we make use of new data and advances in EOS technology to generate a new equation of state for fluid carbon dioxide, which is an improvement over the Span–Wagner EOS in some respects. Further refinements are desirable in order to improve the behavior in certain areas, but resource limitations prevent that at present. The equation of state presented in this report is offered as an alternative to the Span–Wagner EOS, and may be particularly attractive for users who desire faster computations.

Table 1. Physical constants and characteristic properties of carbon dioxide (CO_2)

Quantity	Symbol	Value	Reference
Molar gas constant	R	8.314 462 618 J mol^{-1} K^{-1}	Mohr et al. [13]
Molar mass	M	44.0095 g mol^{-1}	IUPAC [12]
Critical temperature	T_c	304.1282 K	This work and [14]
Critical pressure	p_c	7.377 03 MPa	This work
Critical density	ρ_c	10.6249 mol L^{-1}	This work
Triple-point temperature	T_t	216.5909 K	Kawamura et al. [15]
Triple-point pressure	p_t	0.517 95 MPa	This work
Acentric factor	ω	0.2249	This work

2. Physical Constants and Characteristic Properties

Table 1 lists the most important physical constants and point properties relevant to the development of the new carbon dioxide equation of state, including some properties calculated from the new equation. The molar mass is calculated from the standard values given for carbon and oxygen in the "2007" IUPAC (International Union of Pure and Applied Chemistry) atomic weight evaluation [12]; later IUPAC evaluations replace these standard values with ranges and rounded conventional values that are less useful for calculations such as those here.

Among the critical properties, the most important for developing the equation of state is the critical temperature T_c, which serves as a reducing parameter in the EOS. Once the value of T_c is chosen, the critical density ρ_c and critical pressure p_c are typically left to be determined in the EOS fit, at least if there are sufficient experimental data near the critical point. T_c and p_c are strongly coupled, since the slope of the vapor-pressure curve provides a change in p_c corresponding to any change in T_c.

Many studies have reported critical parameters for CO_2; Span and Wagner [9] cite a number of sources. In Table 2, we list six recent high-precision determinations; for the first four in the table the original T_c was reported on the International Practical Temperature Scale of 1968 (IPTS-68) and the values in Table 2 have been converted to the International Temperature Scale of 1990 (ITS-90) [16, 17]. Moldover [18, 19] determined T_c in two independent ways. The 1974 work used direct optical determination, while the 1979 work derived the critical temperature based on theory-guided analysis of the gravity-induced density profile in a fluid sample very near the critical point. Abdulagatov et al. [20] based their analysis on measurements of the isochoric heat capacity in the two-phase region near the critical point. Duschek et al. [14] based their analysis on coexisting vapor and density measurements near the critical point; their value (converted to ITS-90) was adopted by Span and Wagner [9]. Nowak et al. [21] revised the analysis of Duschek et al. and added a bit more near-critical data, recommending a slightly higher value of T_c. Finally, Kurzeja et

Table 2. Selected literature values for the critical parameters of CO_2

Reference	T_c (K)	p_c (MPa)	ρ_c (kg m^{-3})
Moldover (1974) [18]	304.119		467.8
Moldover et al. (1979) [19]	304.122	7.375	467.0
Duschek et al. (1990) [14] [a]	304.1282	7.3733	467.6
Abdulagatov et al. (1994) [20]	304.1272		467.7
Nowak et al. (1997) [21]	304.134	7.3783	467.6
Kurzeja et al. (1999) [22]	304.1363	7.378491	

[a] Values adopted by Span and Wagner [9].

al. [22] used a highly pure sample and derived T_c from analysis of the differential pressure between two near-critical isochores.

The variation of T_c shown in Table 2 is small, although in many cases the disagreement is larger than the uncertainties claimed by the authors. Issues such as sample purity and the influence of gravity could account for some of the differences. Since there is no compelling reason to prefer any one result, we choose a value of T_c = 304.1282 K. This has the advantage of being identical to the value used by Span and Wagner [9], so that comparisons of the representation of near-critical data are not distorted.

The critical density and pressure for the equation of state were not fixed in advance; they were allowed to adjust to give the best overall fit to properties in the critical region. The critical density given in Table 1 is, when converted to mass units, 467.597 kg m^{-3}, essentially identical to that used in [9]. The value of p_c in Table 1 lies within the range of the experimental determinations listed in Table 2.

The triple-point temperature was recently measured to a standard uncertainty of 0.36 mK by Kawamura et al. [15]. This value agrees within mutual uncertainties with previous high-precision measurements such as those of Head et al. [23] and Pavese and Ferri [24].

3. The Equation of State

3.1. Form of the Equation of State

Like most modern equations of state, our EOS is constructed as a fundamental thermodynamic potential in the form of the molar Helmholtz energy (denoted by a) as a function of absolute temperature T and molar density ρ. This construction allows all other thermodynamic properties (pressure, entropy, heat capacity, sound speed, etc.) to be calculated by straightforward differentiation and combination of terms, as described elsewhere [25]. The use of a single potential to compute all properties guarantees full thermodynamic consistency; it also allows data for properties that cannot be measured very accurately (such

as the isobaric heat capacity) to be predicted with better accuracy based on measurements of other quantities (such as the speed of sound).

The fundamental equation for the molar Helmholtz energy a is the sum of a term representing properties of the substance in the ideal-gas state, a°, and a residual term, a^r, representing effects of intermolecular interactions:

$$a(T,\rho) = a^\circ(T,\rho) + a^\mathrm{r}(T,\rho). \tag{1}$$

Because it is more convenient to work in reduced variables, the temperature and density are reduced by their values at the critical point and the Helmholtz energy is reduced by RT, resulting in the dimensionless function

$$\alpha(\tau,\delta) \equiv \frac{a(T,\rho)}{RT} = \frac{a^\circ(T,\rho) + a^\mathrm{r}(T,\rho)}{RT} = \alpha^\circ(\tau,\delta) + \alpha^\mathrm{r}(\tau,\delta), \tag{2}$$

where α is the reduced Helmholtz energy, $\tau = T_\mathrm{c}/T$ is the reciprocal reduced temperature, and $\delta = \rho/\rho_\mathrm{c}$ is the reduced density. The critical temperature T_c and critical density ρ_c for carbon dioxide are given in Table 1.

3.2. Ideal-gas Term

The ideal-gas contribution to the reduced Helmholtz energy is written as

$$\alpha^\circ(\tau,\delta) = \frac{a^\circ(T,\rho)}{RT} = \frac{h_0^\circ}{RT} - \frac{s_0^\circ}{R} - 1 + \ln\frac{\delta\tau_0}{\delta_0\tau} - \frac{\tau}{R}\int_{\tau_0}^{\tau}\frac{c_p^\circ}{\tau^2}\mathrm{d}\tau + \frac{1}{R}\int_{\tau_0}^{\tau}\frac{c_p^\circ}{\tau}\mathrm{d}\tau, \tag{3}$$

where c_p° is the ideal-gas isobaric heat capacity and τ_0 and δ_0 are the reduced reciprocal temperature and reduced density at an arbitrary reference state of temperature T_0 and density ρ_0, where the ideal-gas enthalpy and entropy are h_0° and s_0°.

Equation (3) requires a formula for the ideal-gas isobaric heat capacity, $c_p^\circ(T)$. Span and Wagner [9] fitted their $c_p^\circ(T)$ to calculated values obtained from a 1986 private communication from a researcher at Texas A&M University; to our knowledge that work was never published. Today, for small molecules it is possible to obtain very accurate $c_p^\circ(T)$ by calculating it directly from a partition function based on state-of-the-art spectroscopic information. This was done for the CO_2 molecule (all 12 isotopologues, then weighted to produce results for the natural isotopic abundances) by Tashkun and Harvey [26, 27]. We fitted their results to the following functional form:

$$\frac{c_p^\circ(T)}{R} = n_0^\circ + \sum_{i=1}^{5} n_i^\circ \left(\frac{m_i^\circ}{T}\right)^2 \frac{\exp\left(m_i^\circ/T\right)}{\left[\exp\left(m_i^\circ/T\right) - 1\right]^2}, \tag{4}$$

which when substituted into Eq. (3) and rewritten in terms of dimensionless quantities produces this expression for the ideal-gas Helmholtz energy:

$$\alpha^\circ(\tau,\delta) = \ln\delta + n_6^\circ + n_7^\circ\tau + (n_0^\circ - 1)\ln\tau + \sum_{i=1}^{5} n_i^\circ \ln\left[1 - \exp\left(-\frac{m_i^\circ\tau}{T_\mathrm{c}}\right)\right]. \tag{5}$$

Table 3. Values of parameters for Eq. (5).

i	n_i°	m_i°
0	3.500 11	
1	1.6429	946.0
2	0.4	1063.0
3	1.0196	1985.0
4	1.027	3502.0
5	0.202	10 884.0
6	−6.125 109 366 639 762 2	
7	5.115 566 048 749 188 1	

The parameters in Eq. (5) are listed in Table 3.

The values of n_6° and n_7° were adjusted to fix the arbitrary zeros of the enthalpy and entropy scales; calculations for real thermodynamic processes are independent of these values. Here, we adopt the reference state that is common in the refrigeration industry; for the saturated liquid at 273.15 K the enthalpy is taken as 200 kJ/kg and the entropy is taken as 1 kJ/(kg K). We note that this differs from the ideal-gas reference state used by Span and Wagner [9].

One subtle point is that, because the ideal-gas term is based on a molecular partition function, the corresponding temperatures are on the thermodynamic temperature scale. The real-fluid equation of state, however, is fitted to data whose temperatures are on the International Temperature Scale of 1990 (ITS-90) [16] and therefore is considered to be a function of temperatures on that scale. Estimates have been published for the small differences between thermodynamic temperature and ITS-90 [28, 29]. The effect of these differences should be negligible for the purposes of any practical thermodynamic calculation, but they may be significant compared to the small uncertainties attained for c_p°.

3.3. Real-fluid Equation of State

The residual contribution to the reduced Helmholtz energy is written as

$$\alpha^{\mathrm{r}}(\tau,\delta) = \frac{a^{\mathrm{r}}(T,\rho)}{RT} = \sum_{i=1}^{I_{\mathrm{Pol}}} n_i \delta^{d_i} \tau^{t_i} + \sum_{i=I_{\mathrm{Pol}}+1}^{I_{\mathrm{Pol}}+I_{\mathrm{Exp}}} n_i \delta^{d_i} \tau^{t_i} \exp\left(-r_i \delta^{l_i}\right) + \sum_{i=I_{\mathrm{Pol}}+I_{\mathrm{Exp}}+1}^{I_{\mathrm{Pol}}+I_{\mathrm{Exp}}+I_{\mathrm{GBS}}} n_i \delta^{d_i} \tau^{t_i} \exp\left[-\eta_i (\delta-\varepsilon_i)^2 - \beta_i (\tau-\gamma_i)^2\right], \quad (6)$$

where $I_{\mathrm{Pol}} = 5$, $I_{\mathrm{Exp}} = 7$, and $I_{\mathrm{GBS}} = 12$ are respectively the number of polynomial, exponential, and Gaussian bell-shaped terms in Eq. (6). The parameters of Eq. (6) resulting from the EOS optimization process are given in Table 4.

Table 4. Values of parameters in Eq. (6)

i	n_i	t_i	d_i	l_i	r_i	η_i	β_i	γ_i	ε_i
1	0.032 646 485	1	4						
2	0.828 749 590 01	0.16	1						
3	−0.718 938 788 655	1.1369	1						
4	−0.842 769 989 070 51	1.1	2						
5	0.109 225 7	0.4217	3						
6	−0.892 02	2.514	1	2	1.1368				
7	−0.5989	3.666	3	2	1.182				
8	1	1	2	1	0.81				
9	−0.013 545	1.219	7	2	0.666				
10	−0.005 117 2	7.25	1	3	1				
11	−0.034 668	8	2	3	0.7514				
12	−0.394 52	0.7	1	2	0.4656				
13	−0.188	2.7	2			1.682	2.655	1.398	−0.1762
14	0.227 05	2.4	1			1.7558	0.567	1.3241	0.4031
15	0.225 18	2.582	1			1.8562	2.249	1.245 15	0.771 85
16	−0.340 52	0.536	1			1.337	0.74	1.2006	−0.0849
17	−0.1	1.46	1			1	2.34	1.1453	0.6133
18	0.190 96	1.2	1			1.864	2.3	0.9526	0.0379
19	−0.257 846 5	1.0305	1			0.9388	0	1	1.0626
20	−0.191	1	2			10.35	60.79	1.3085	0.652
21	−0.022 783	1	2			10.52	327	1.1085	0.8918
22	−0.0005	1	2			43	22 000	1.0131	0.972
23	−0.000 004 4	1	2			200	60 000	1.005	0.9
24	−0.000 084 8	1	2			250	1 000 000	1.0024	0.978

3.4. Fitting the Equation of State

The parameters in Eq. (6) were fitted to a variety of experimental data. The use of a Helmholtz potential allows different types of data (sound speeds, densities, virial coefficients, heat capacities, vapor pressure, etc.) to be considered simultaneously. The fitting algorithm was originally described by Lemmon and Jacobsen [30] and has been refined through the years to better constrain the behavior of the EOS; a recent summary is given by Akasaka and Lemmon [31].

When necessary, input temperatures were converted to the ITS-90 scale using established procedures [17, 32]. A small adjustment due to change in temperature scales was also made for older heat-capacity data that depend on measuring a temperature difference [32].

4. Comparisons with Data

A thorough overview of experimental data for CO_2 thermodynamic properties was given by Span and Wagner [9]. We direct readers to that paper for many references that are mainly of historical interest. In the following, we focus primarily on those data sets that were deemed to be the most reliable by Span and Wagner and on high-accuracy data that have appeared since that work. Data of lesser accuracy that cover regions where data are lacking are also used in comparisons. When necessary, experimental temperatures were converted to the ITS-90 scale.

In some cases, we will analyze the agreement of equations of state with experimental data sets in terms of statistics based on the relative deviation of the experimental quantity from that calculated by the equation of state. We define the relative deviation $\Delta_{r,X}$ of a property X for a given data point by:

$$\Delta_{r,X} \equiv \frac{X_{exp} - X_{EOS}}{X_{EOS}}, \tag{7}$$

We can then define the average absolute relative deviation (AARD) and Bias for each data set as

$$\text{AARD} = \frac{1}{N}\sum_{i=1}^{N} |\Delta_{r,X,i}|, \tag{8}$$

$$\text{Bias} = \frac{1}{N}\sum_{i=1}^{N} \Delta_{r,X,i}, \tag{9}$$

where N is the number of data points.

4.1. Ideal-gas Heat Capacity

While in principle the ideal-gas heat capacity could be obtained by extrapolating gas-phase heat-capacity measurements to zero pressure or from analysis of gas-phase sound-speed data, for small molecules such as CO_2 an approach based on molecular physics is much more accurate. Information on molecular energy levels is obtained from spectroscopic information, and either used directly or used as input to a molecular model in order to construct a partition function for the molecule. Appropriate manipulations then yield thermochemical quantities such as $c_p^\circ(T)$. A state-of-the-art calculation with this approach was performed by Tashkun and Harvey [26, 27], and their values for CO_2 of natural isotopic composition were fitted by Eq. (4).

In Fig. 1, we show the deviations of our EOS and of the Span–Wagner EOS from the calculated values of Tashkun and Harvey. The new EOS represents the high-accuracy calculations much better than the Span–Wagner EOS (which was fitted to older, less accurate, undocumented molecular calculations). There is some small room for improvement above 1000 K, but the magnitude of the error is smaller than the accuracy of any conceivable heat-capacity measurement.

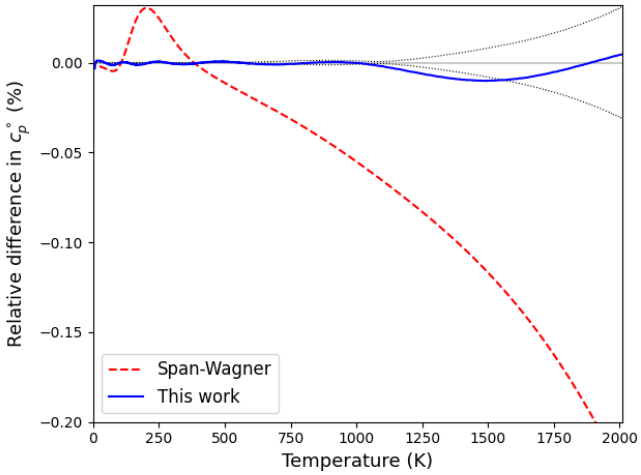

Fig. 1. Deviations of the present EOS [Eq. (4)] and the Span–Wagner ideal-gas formulation from the calculations of Tashkun and Harvey [26, 27] for c_p°. Dashed lines represent expanded (k = 2) uncertainty of calculated values.

4.2. Virial Coefficients

The virial expansion is a systematic series of corrections to the ideal-gas law in powers of the molar density ρ. It is written as

$$\frac{p}{\rho RT} = 1 + B(T)\rho + C(T)\rho^2 + \ldots, \tag{10}$$

where the second virial coefficient $B(T)$ is rigorously related to the interactions between two molecules, $C(T)$ represents interactions among three molecules, etc. At low and moderate pressures, accurate values of B and C will produce accurate gas-phase properties.

A major source of $B(T)$ for our fitting was the calculated values of Hellmann [33], which span a temperature range from 150–2000 K and were shown to agree well with the best experimental data in the range where good data existed. These calculations were later extended down to 75 K and up to 3000 K [34], although the high end of this temperature range is less physically meaningful because the real molecule will undergo significant dissociation.

Figure 2 shows the behavior of $B(T)$ over a wide range; our new EOS is in good agreement with Hellmann's values over most of this range, especially at high temperatures where Span and Wagner have a clearly incorrect temperature dependence. Span and Wagner perform better for B in a range of temperatures from about 250–350 K, where their EOS was constrained by the accurate experimental data of Duschek et al. [35] (which were also used to optimize the pair potential developed by Hellmann [33]). The differences near 200–250 K are not as large as they might seem because of the large negative magnitude of B; they are less than 1 % in relative terms. The expanded uncertainties of Hellmann's

calculated values (see Appendix A) are 0.5 cm^3 mol^{-1} for most of the temperatures in Fig. 2, with larger uncertainties at high and low temperatures; the differences from our EOS all lie within those expanded uncertainties. For Hellmann's B at lower temperatures, the relative deviations of our EOS values are less than 5 % down to approximately 100 K, and the EOS is in qualitative agreement to the lowest calculated temperature of 75 K.

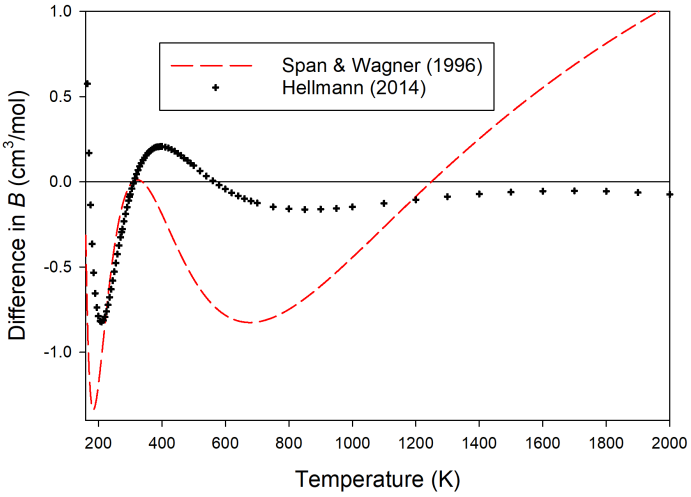

Fig. 2. Difference from new EOS of values of B from Hellmann [33] and calculated by the EOS of Span and Wagner [9].

Figure 3 shows the differences from our EOS of selected high-quality experimental determinations of B [35–42]. In the limited range where experimental data exist, the agreement is good within the scatter of the data.

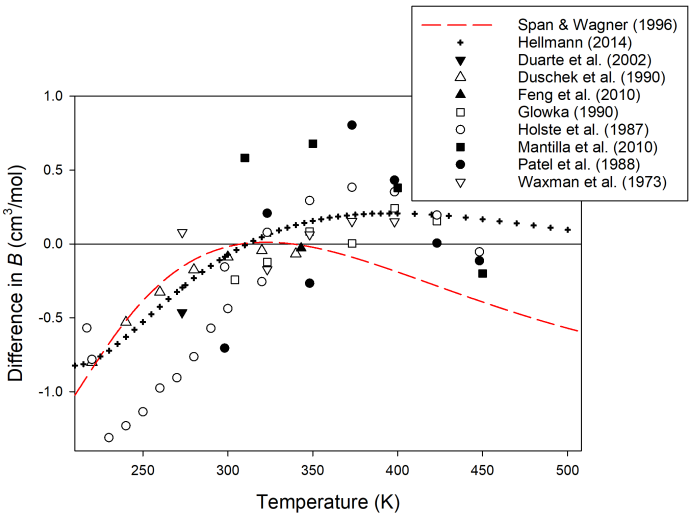

Fig. 3. Deviation from the new EOS of experimental values [35–42] of B and of those from Hellmann [33] and the Span–Wagner EOS.

The third virial coefficient C is more difficult to measure; some data exist but with much more scatter and uncertainty than for $B(T)$. Values of $C(T)$ have also been calculated by Hellmann based on a three-body potential [43] in addition to the two-body potential [33] used to calculate B. Hellmann's original calculations had a lower temperature limit of 190 K; the calculations were later extended to 140 K and the additional data are available in [34].

In Fig. 4, we plot $C(T)$ as given by our EOS, by the Span–Wagner EOS [9], as calculated from the *ab initio* molecular model of Hellmann [43], and from several experimental sources [35–41]. Error bars are shown for the calculations of Hellmann; estimation of these expanded (k = 2) uncertainties is described in Appendix A. Most of the experimental sources did not report uncertainties in C; the exception is the work of Duschek et al. [35] whose data agree with the calculated values of Hellmann (and with our EOS) within mutual uncertainties. Both our EOS and that of Span and Wagner are consistent with experimental results within their scatter, but our new EOS is in much better agreement with theoretical $C(T)$ below 250 K. The Span–Wagner values are also slightly inconsistent with the theoretical $C(T)$ above 400 K.

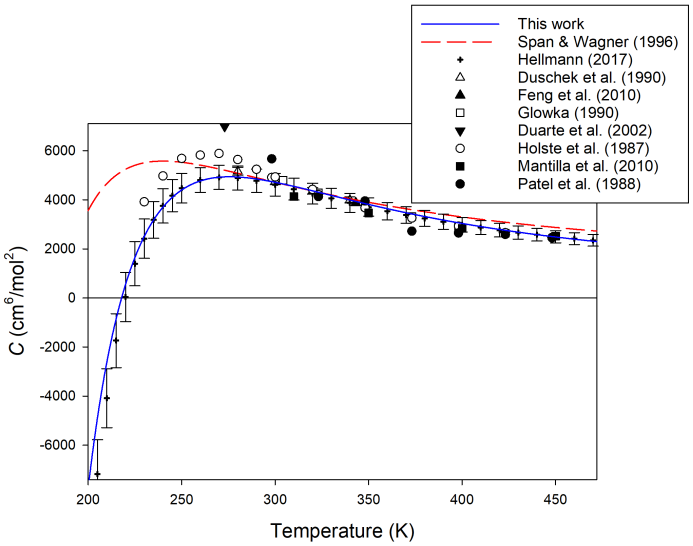

Fig. 4. Experimental [35–41] and predicted values of the third virial coefficient C.

4.3. Saturated Vapor Pressure

One of the most important thermodynamic properties for applications is the vapor pressure. Span and Wagner reviewed many data sources, ultimately relying in large part on the careful measurements of Duschek et al. [14]. We made a similar choice, supplementing those data by measurements in a metrological context at 273.16 K [44, 45], some more recent metrological measurements [46], and a value near the critical temperature from Nowak et al. [21]. The data of Kartal Dogan et al. [46], not tabulated in the original paper, were obtained and archived by Harvey [34].

Figure 5 shows the deviations of these data from the new EOS, along with the Span–Wagner EOS. Both EOS agree closely with experiment, generally within 0.01 %. There may be some room for improvement in the range 220–260 K, but it is difficult to say with the scatter of the data.

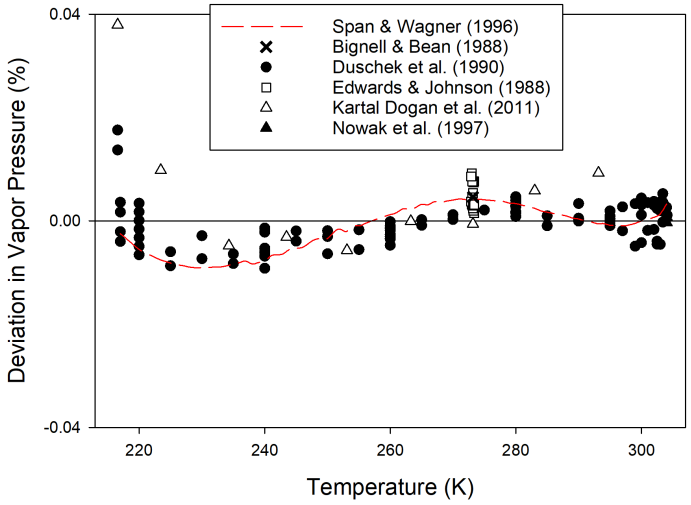

Fig. 5. Deviation of selected experimental vapor pressures [14, 21, 44–46] from the new EOS.

4.4. Saturated Densities

The densities of the coexisting phases along the vapor–liquid saturation boundary are good indicators of the performance of the EOS. The most accurate measurements are for the liquid phase; the EOS is compared with selected experimental sources [14, 21, 47–49] in Fig. 6. Both our EOS and that of Span and Wagner [9] reproduce the experimental data well, particularly those of Duschek et al. [14]. The greater scatter of data at the highest temperatures is expected, due to the difficulty of making measurements close to the critical point. There are systematic deviations for the data of Haynes [47]; we have chosen to follow the data of Duschek et al. instead (Span and Wagner made the same choice).

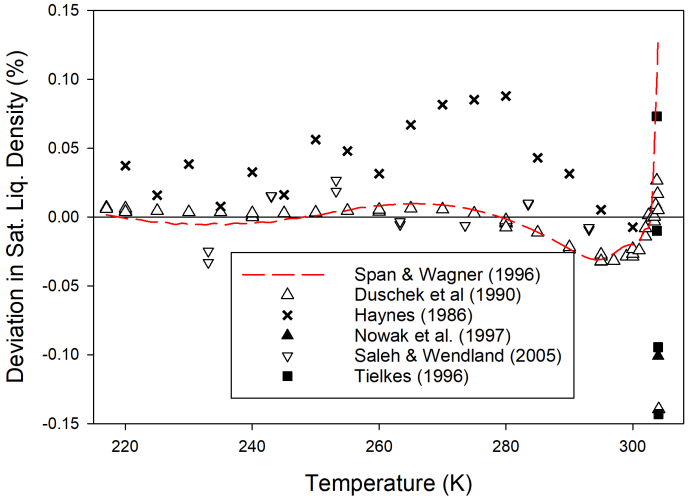

Fig. 6. Deviation from the new EOS of selected experimental values [14, 21, 47–49] of the saturated liquid density.

There are fewer data for the saturated vapor; Fig. 7 shows that we agree well with the data of Duschek et al. [14]. As expected, there is again more uncertainty near the critical temperature.

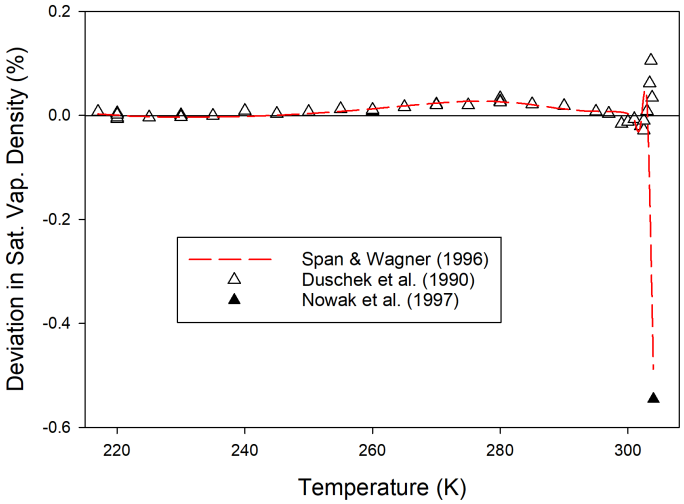

Fig. 7. Deviation from the new EOS of selected experimental values [14, 21] of the saturated vapor density.

4.5. Density

There are many different sources of measurements for the density of carbon dioxide in various states; a full review is impractical. Span and Wagner reviewed most of the data

available prior to their publication [9]. Here, we focus on the data sets that most effectively constrain the equation of state, either because of their high accuracy or because they cover a region in which few other data exist. Omission of a source from the graphs does not mean that the data were not considered in our work.

For clarity, we separately examine data at vapor-like and liquid-like densities. Since density varies continuously with pressure at supercritical temperatures, we choose an arbitrary boundary of 12 mol/L for these comparisons. We will also separately consider data at high temperatures (above 500 K) and omit data very near the critical point.

Figure 8 shows the percent deviations from each EOS for selected sources of experimental data in the lower density range as a function of temperature, and Fig. 9 shows the same data as a function of pressure. Many of the best data come from a series of measurements in the same group at the Ruhr University of Bochum [21, 35, 50, 51]; these are plotted together as “Bochum” and we note that Span and Wagner depended heavily on these data. The entry “Ruhrgas” designates two sets of density data measured by two different methods and communicated by Jaeschke [52, 53]. Several other sources of high-accuracy data are also plotted [36, 38–40, 54–56].

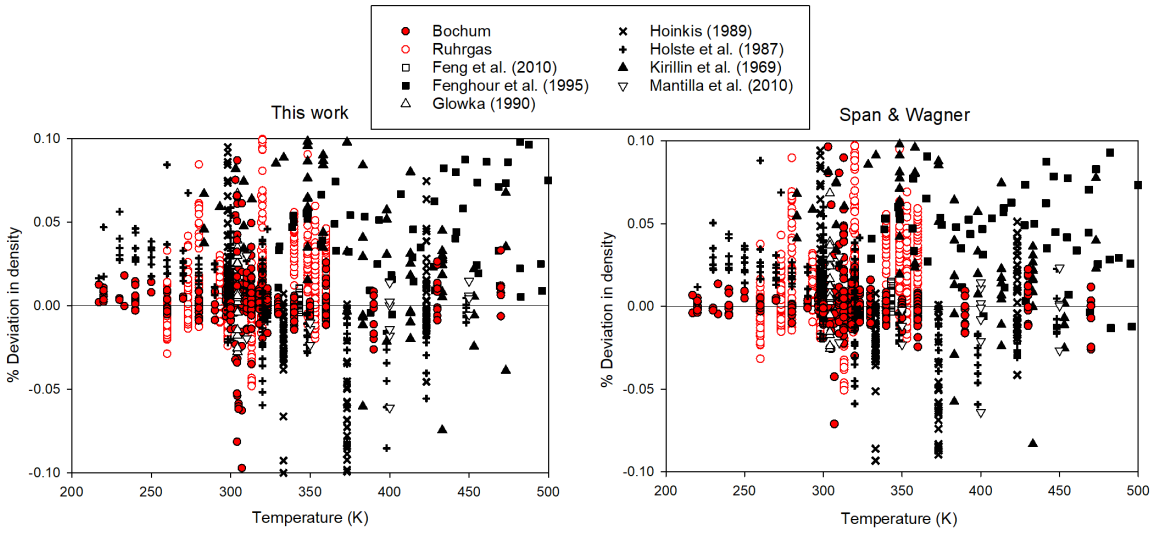

Fig. 8. Deviations of selected experimental density data from the new EOS and that of Span and Wagner for densities below 12 mol/L, as a function of temperature.

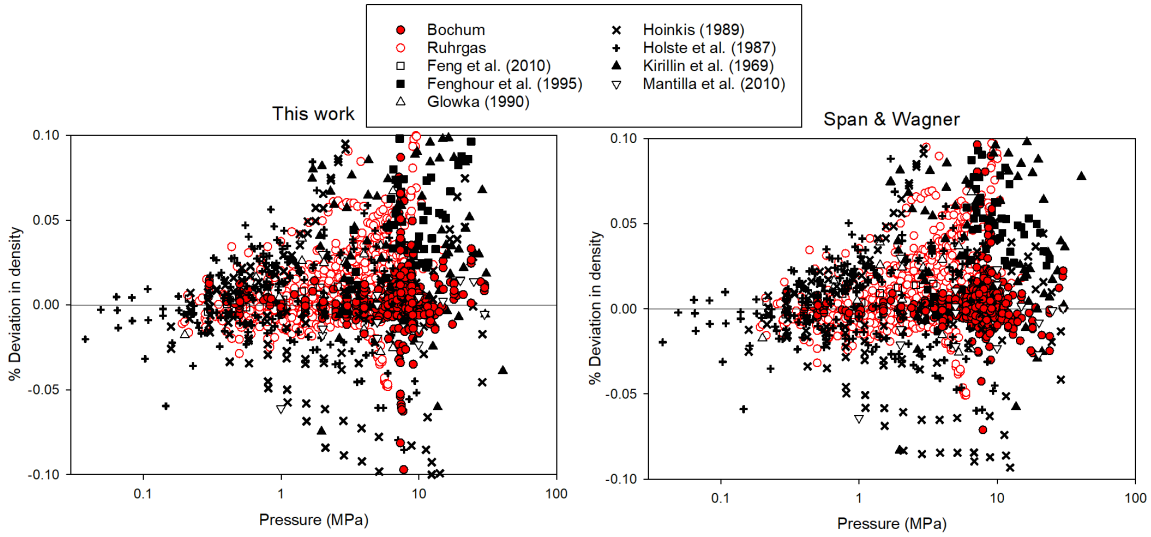

Fig. 9. Deviations of selected experimental density data from the new EOS and that of Span and Wagner for densities below 12 mol/L, as a function of pressure.

In both figures, the right and left panels are very similar, indicating that both EOS fit the experimental density data equally well. The data from Bochum are described within 0.01 % for the most part. We note that the increased scatter near 304 K and 7.4 MPa represents data near the critical point, where experimental measurements are more difficult and the density is sensitive to small changes in temperature or pressure. In a few cases, mostly near the critical point, points are not shown on the figures because they are off the vertical scale of the plots.

Data at higher densities are represented in a similar manner in Figs. 10 and 11. The same sources are lumped together under “Bochum” and “Ruhrgas” as in Figs. 8 and 9. Both equations of state perform similarly well, but the new EOS does a slightly better job on the high-accuracy Bochum data, representing most of them within 0.02 % (AARD 0.006 %, Bias −0.0004 %) while the corresponding scatter for the Span–Wagner EOS is almost twice as large (AARD 0.010 %, Bias −0.003 %). The new EOS also better represents the precise high-pressure data of Mantilla et al. [36], which were not available when the Span–Wagner EOS was developed (AARD 0.017 %, versus 0.033 % for Span–Wagner). Representation of the other data sets shown [40, 55–61] is generally of similar quality.

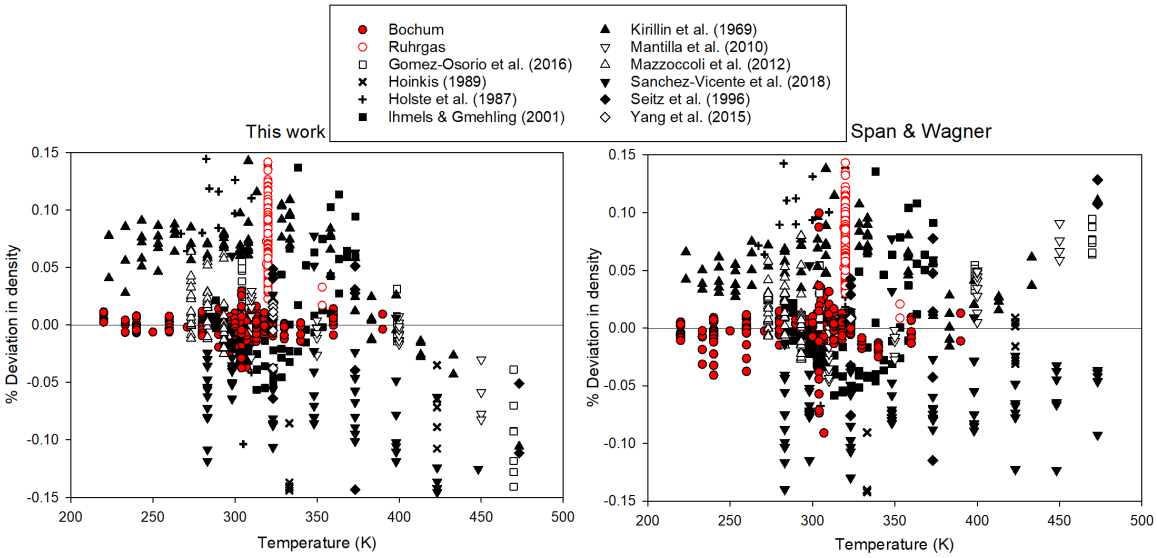

Fig. 10. Deviations of selected experimental density data from the new EOS and that of Span and Wagner for densities above 12 mol/L, as a function of temperature.

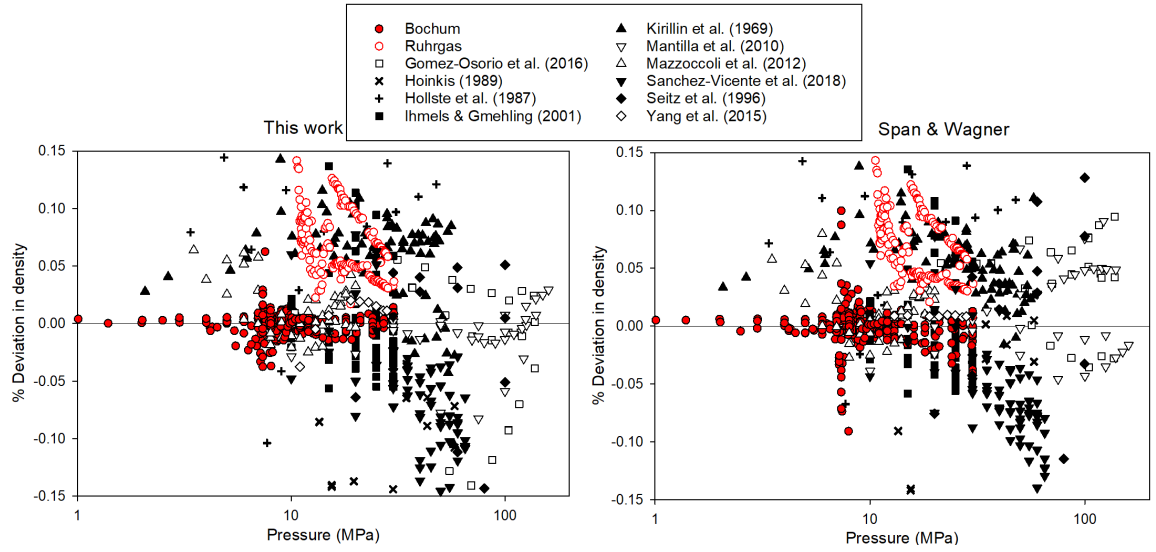

Fig. 11. Deviations of selected experimental density data from the new EOS and that of Span and Wagner for densities above 12 mol/L, as a function of pressure.

It is evident from Fig. 10 that there may be some systematic deviations of the new EOS above 400 K, but the experimental data are too scattered to be able to draw firm conclusions.

Experimental data are much sparser above 500 K. The only high-accuracy “Bochum” data available are an isotherm at 523 K from the thesis of Brachthäuser [62]; the data are given

in an Appendix of [50]. We have lumped together for plotting purposes data from three papers of Vukalovich and coworkers [63–65], one of which extends above 1000 K. The data of Shmonov and Shmulovich [66] extend to almost 1000 K with pressures up to 800 MPa. Two other sources [54, 67] extend to moderately high temperatures.

Figures 12 and 13 show the deviations of these sources from the two equations of state. The differences are mostly insignificant. Both EOS agree well with the accurate isotherm from Bochum at 523 K. Agreement with the measurements of Fenghour et al. [54] is better for the Span–Wagner EOS (AARD of 0.036 % for points above 500 K, compared to 0.065 % for the new EOS), but this difference is within the 0.05–0.1 % uncertainty stated for the data. The Vukalovich data are mostly reproduced within 0.3 %, with more scatter for the high-pressure Schmonov data.

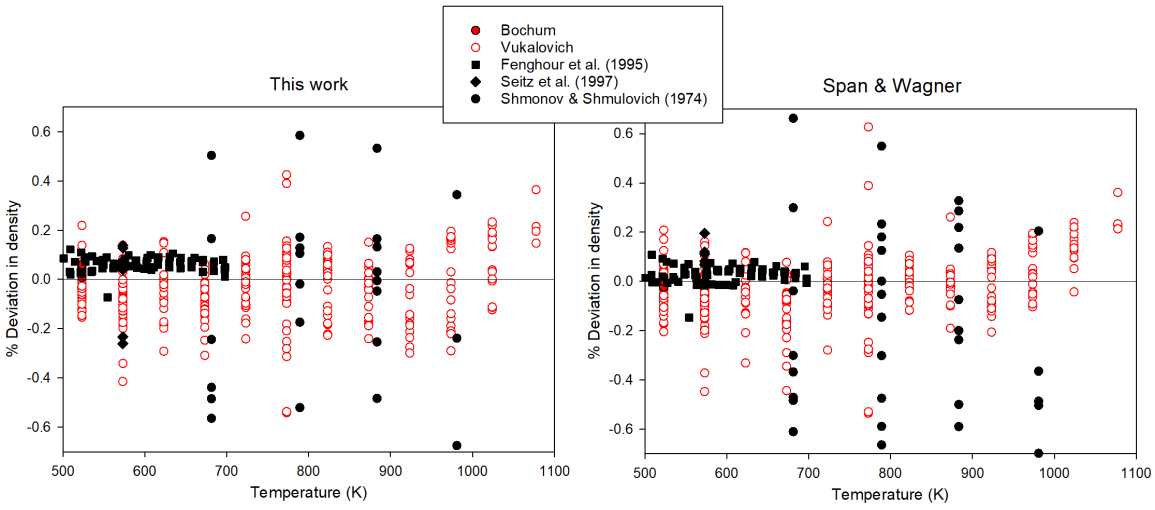

Fig. 12. Deviations of selected experimental density data above 500 K from the new EOS and that of Span and Wagner, as a function of temperature.

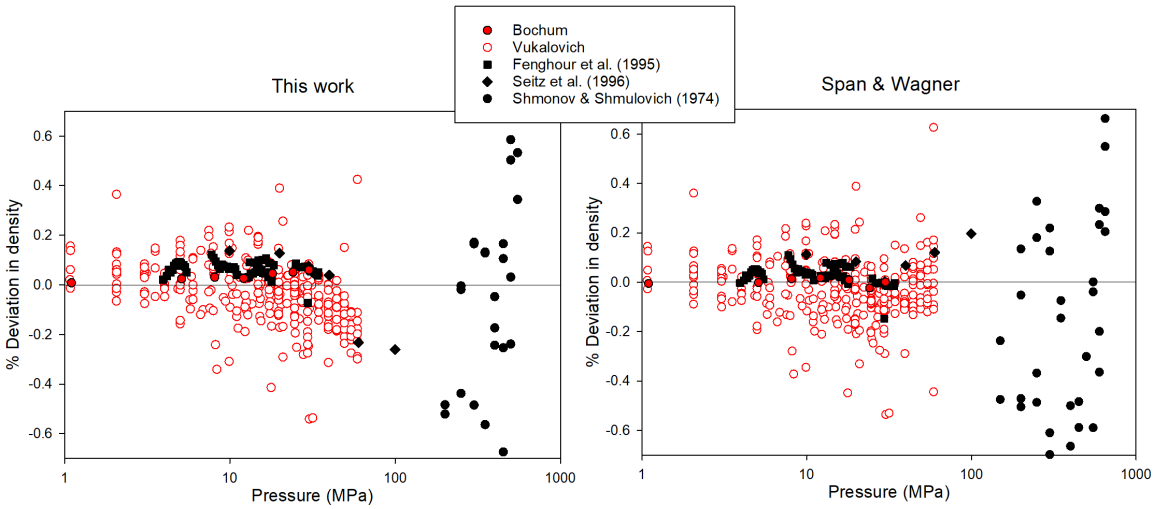

Fig. 13. Deviations of selected experimental density data above 500 K from the new EOS and that of Span and Wagner, as a function of pressure.

4.6. Speed of Sound

Speed-of-sound data provide an important constraint on the equation of state. Even though the property itself is seldom of great technical importance, it combines both volumetric and caloric derivatives related to the expansivity and heat capacity of the fluid. Getting the sound speed correct is a means to ensure that quantities that are more difficult to measure accurately, such as heat capacities, are correct.

Table 5 presents the AARD and Bias (along with the number of data points N) for the different data sets as computed by both the new EOS and the Span–Wagner EOS. We exclude the very scattered data of Novikov and Trelin [68, 69] that are shown graphically and discussed below.

At gas-like densities, the only data Span and Wagner had to work with were a few high-quality acoustic resonance measurements from Lemming [73] and data from two older papers by Novikov and Trelin [68, 69], which we will plot together with the label “Novikov.” Importantly, there are now three newer sources of high-accuracy gas-phase sound-speed data from acoustic resonance methods [70, 71, 75].

In Figs. 14 and 15, we show the deviations of sound-speed data at gas-like densities from both our EOS and that of Span and Wagner. The accurate resonance data (most of which were unavailable to Span and Wagner) are shown with red symbols. We note that there are many additional “Novikov” points (at least as many as are visible on the figures) with positive deviations higher than the 0.2 % chosen as the upper limit for Figs. 14 and 15.

Table 5. Comparison for speed-of-sound data

		This work		Span and Wagner	
First author	N	AARD (%)	Bias (%)	AARD (%)	Bias (%)
Estrada-Alexanders [70]	59	0.019	−0.004	0.017	0.015
Estrada-Alexanders [71]	123	0.018	0.018	0.024	0.024
Kanischchev [72]	9	1.566	1.062	2.377	2.236
Lemming [73]	50	0.011	0.001	0.014	0.007
Lin [74]	47	0.225	−0.092	0.488	−0.199
Liu [75]	74	0.010	0.010	0.016	0.016
Pecceu [76]	31	0.450	−0.429	0.528	−0.208
Pitaevskaya [77]	176	1.045	−0.647	0.761	−0.020
Rivas [78]	49	0.287	0.189	0.432	0.054

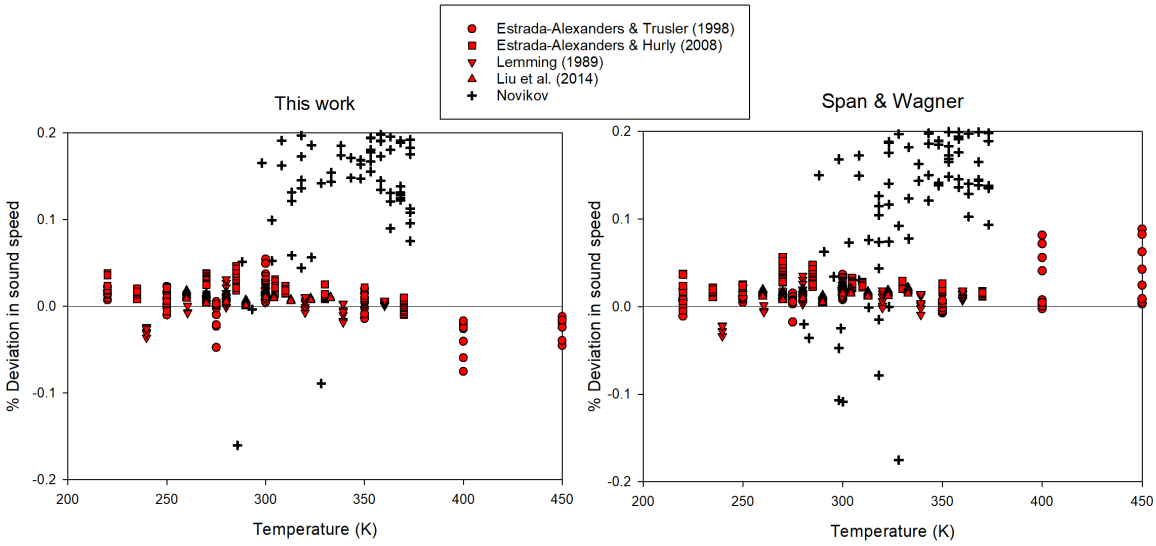

Fig. 14. Deviations of experimental sound-speed data from the new EOS and that of Span and Wagner for densities below 12 mol/L, as a function of temperature.

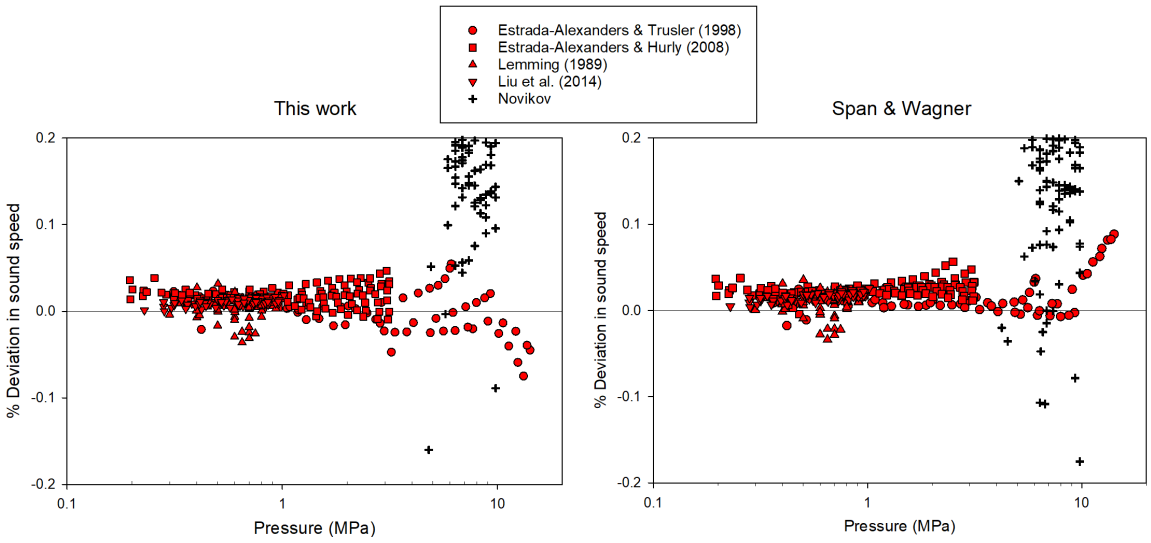

Fig. 15. Deviations of experimental sound-speed data from the new EOS and that of Span and Wagner for densities below 12 mol/L, as a function of pressure.

Both EOS perform similarly well for the high-quality data (the red points), although the new EOS has slightly smaller deviations for most of these data (most visible in Fig. 15; see also Table 5) and is slightly better for the high-temperature points of Estrada-Alexanders and Trusler [70] visible in Fig. 14.

Figures 16 and 17 show similar information for high densities, where there are two new high-quality data sources [74, 78] (shown in red symbols) in addition to the two sources that Span and Wagner mainly relied on for liquid-like densities [76, 77]. We also plot a few points from a 1981 study that extends the pressure range to 800 MPa [72].

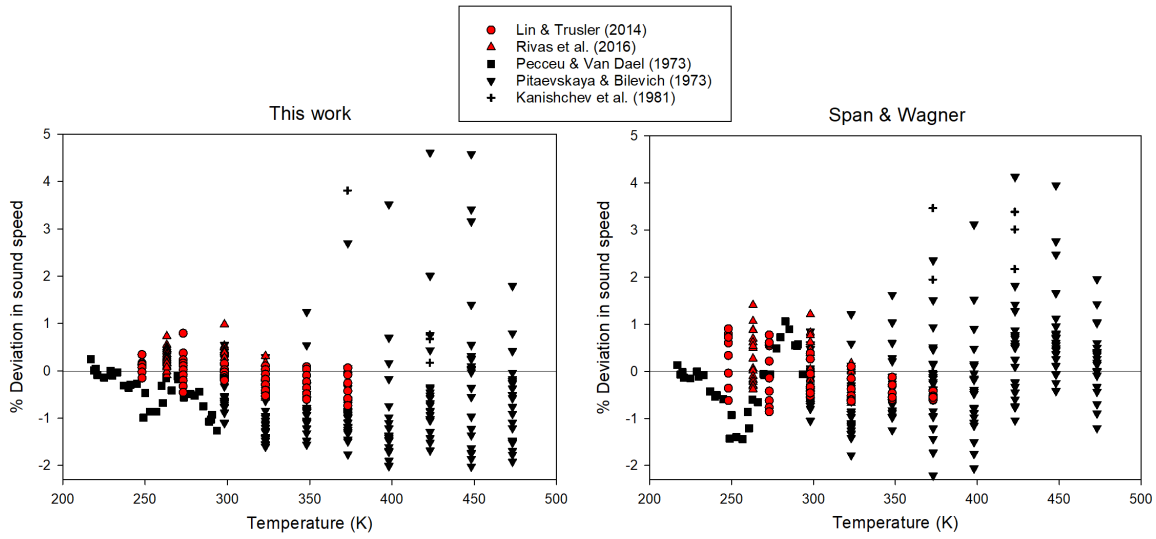

Fig. 16. Deviations of experimental sound-speed data from the new EOS and that of Span and Wagner for densities above 12 mol/L, as a function of temperature.

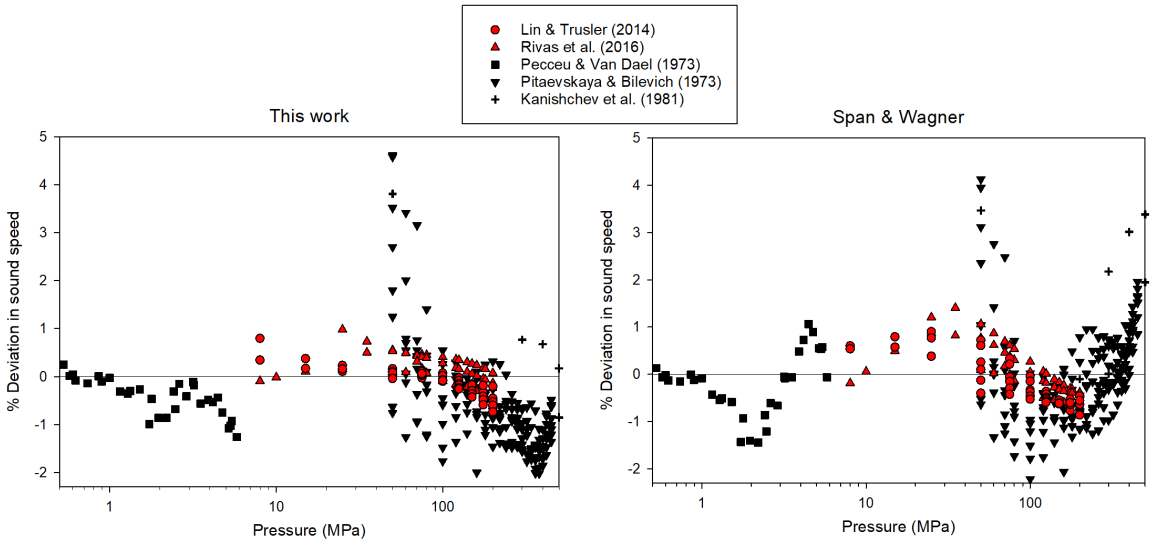

Fig. 17. Deviations of experimental sound-speed data from the new EOS and that of Span and Wagner for densities above 12 mol/L, as a function of pressure.

At these liquid-like densities, some areas of modest improvement can be seen. The new EOS is in significantly better agreement with the two new sources [74, 78] (which were not available to Span and Wagner), although for many points the deviation is still not within the standard relative uncertainty of 0.1 % [74] or approximately 0.2 % [78]. A better representation is obtained of the sound speeds for the saturated liquid measured by Pecceu and

Van Dael [76]. The high-pressure points of Kanischchev et al. [72] are also in somewhat better agreement as can be seen in Table 5.

4.7. Heat Capacities

We first consider the isobaric (constant-pressure) heat capacity, c_p. We will not plot data for this quantity at low pressures, because that would be mostly redundant with the ideal-gas heat capacity c_p° discussed in Sec. 4.1. Even at moderately higher densities, the behavior of c_p is determined by c_p° and the temperature derivatives of the virial coefficients $B(T)$ and $C(T)$ discussed in Sec. 4.2. We therefore limit our comparisons to densities greater than 2 mol/L.

Span and Wagner primarily relied on data from two 1989 papers by Ernst and coworkers [79, 80], where the reported data have relative uncertainties on the order of 1 %, which is good accuracy for heat-capacity measurements on compressed gases. We show these data in red in the figures below. More recently, Ishmael et al. [81] provided data with similar uncertainties. We have also included three additional sources of fair accuracy [82–84], in part to show a wider range of conditions.

Figures 18 and 19 show the deviations of the experimental data from our EOS and from the EOS of Span and Wagner, as a function of temperature and of pressure, respectively. It is evident that there is no significant difference between the two EOS in their representation of these c_p data. Both EOS can reproduce the most accurate data [79–81] approximately within their uncertainties. A few points have deviations off the scale of the figures; these are at states near the critical point where c_p diverges and becomes difficult to measure.

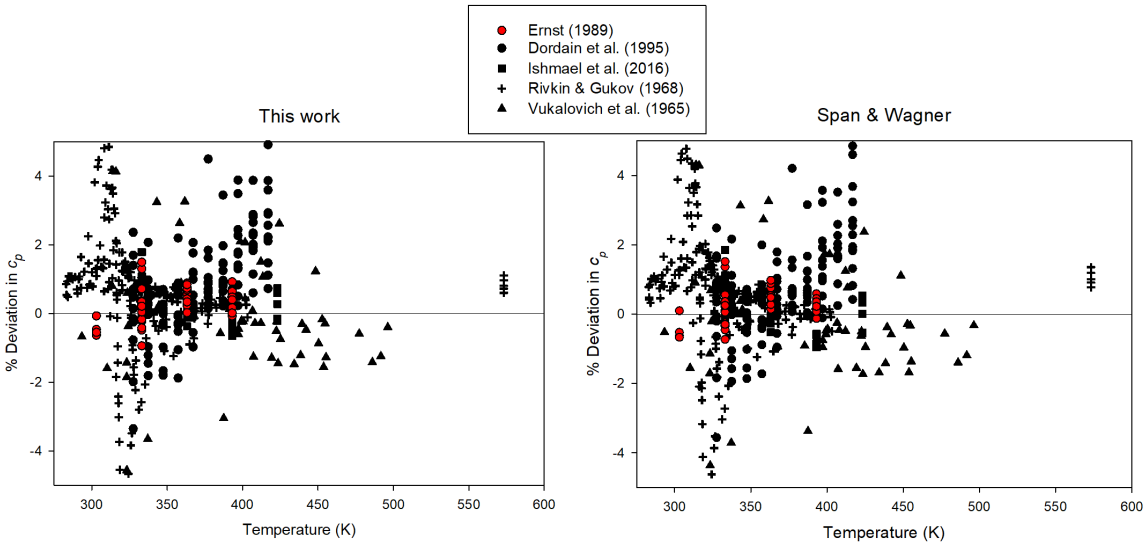

Fig. 18. Deviations of experimental isobaric heat-capacity data from the new EOS and that of Span and Wagner for densities above 2 mol/L, as a function of temperature.

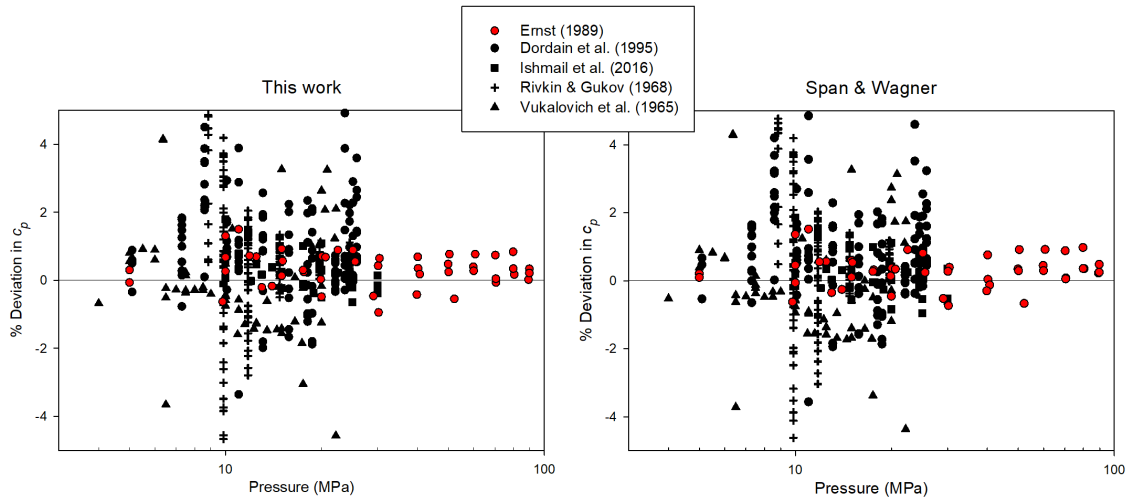

Fig. 19. Deviations of experimental isobaric heat-capacity data from the new EOS and that of Span and Wagner for densities above 2 mol/L, as a function of pressure.

Next, we consider the isochoric (constant-volume) heat capacity c_v. Many of the experimental studies of c_v were focused on studying its weak divergence very near the critical point. In this section, we exclude those studies (which will be considered in Sec. 5) and compare only with those that cover a wider range of conditions. Deviation plots for three wide-ranging studies [85–87] are shown in Figs. 20 and 21.

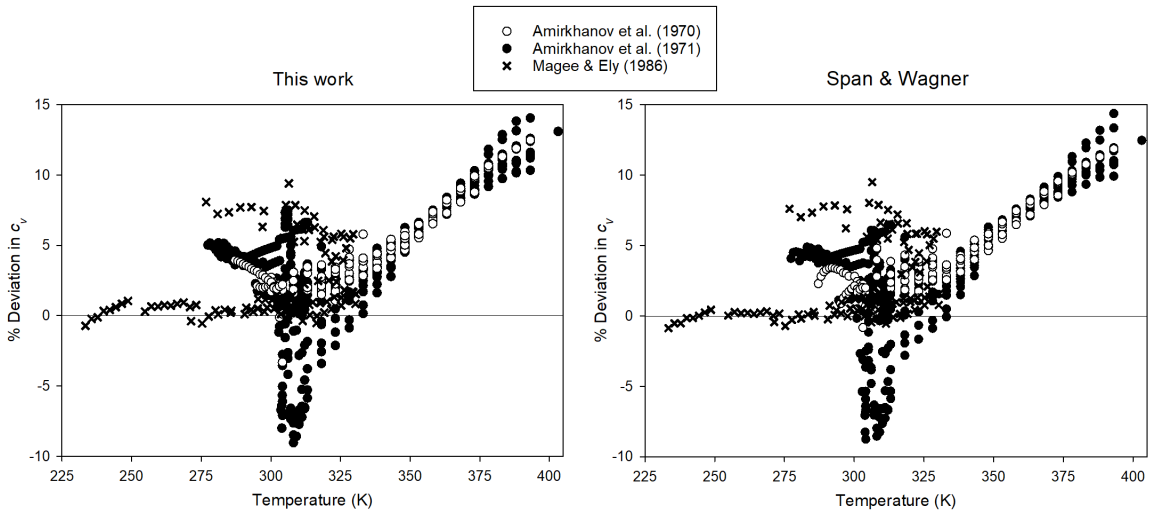

Fig. 20. Deviations of experimental isochoric heat-capacity data from the new EOS and that of Span and Wagner, as a function of temperature.

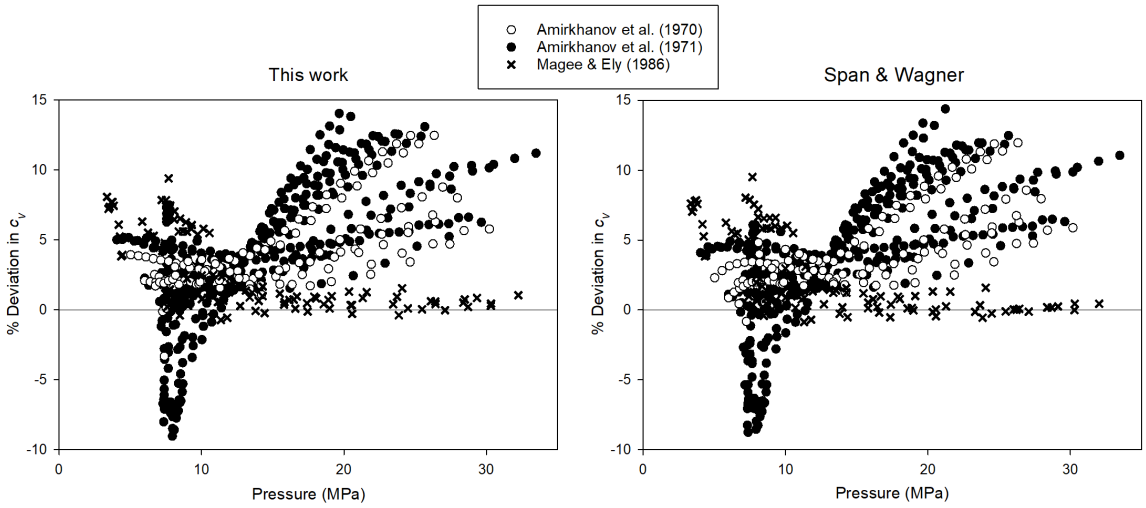

Fig. 21. Deviations of experimental isochoric heat-capacity data from the new EOS and that of Span and Wagner, as a function of pressure.

As was the case with c_p, there is negligible difference between the two EOS in representation of this property. Larger deviations are visible near the critical point, where c_v weakly diverges and measurements are difficult. Both EOS reproduce many (but not all) of the data of Magee and Ely [87] within their claimed uncertainties of 0.5 % in the liquid and 2 % in the vapor. There is a systematic discrepancy with the data reported by Amirkhanov and coworkers [85, 86] at higher temperatures. The fact that the same deviation is observed with two independently fitted EOS, both of which were also fitted to data (such as sound speeds) that are generally measured with more accuracy than c_v, suggests that the problem lies with the reported data.

The isochoric heat capacity can also be measured in the two-phase region, where the quantity represents a combination of the heat capacities of the vapor and liquid phases and the latent heat of vaporization. Several researchers have reported this quantity [85–92]; in most cases the behavior near the critical point was the main interest but some studies [87, 88, 90] covered a wider range of conditions.

In Fig. 22, we plot the deviations of data from the two EOS versus temperature (a pressure plot would be redundant because in the two-phase region pressure is determined by the temperature). For clarity, we exclude the data of Amirkhanov and coworkers [85, 86], which systematically deviate in the positive direction by amounts on the order of 5 %. To avoid distortions very near the critical point, we exclude points at temperatures above 304 K. Some differences near the critical temperature are noticeable between the left and right panels of Fig. 22, but neither EOS can be said to perform better than the other.

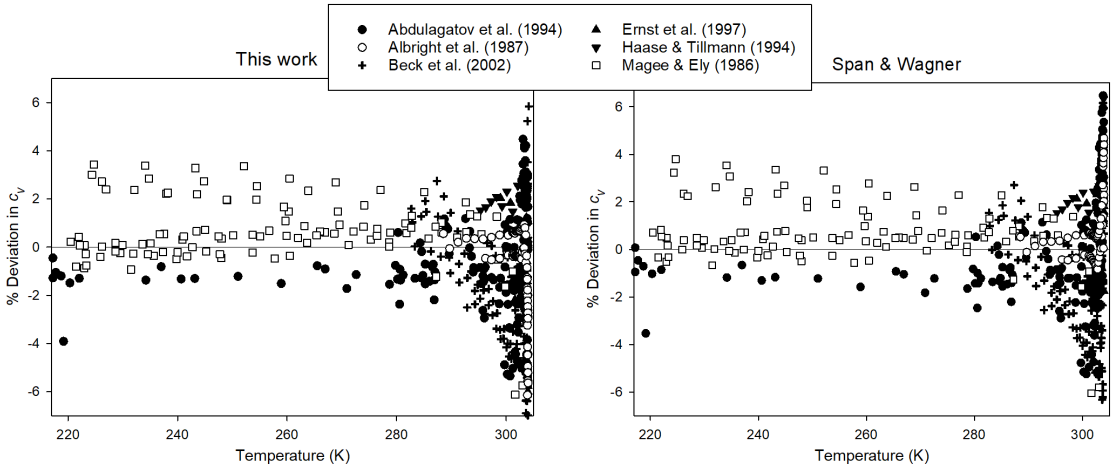

Fig. 22. Deviations of experimental isochoric heat-capacity data in the two-phase region from the new EOS and that of Span and Wagner, as a function of temperature.

5. Behavior Near the Critical Point

The Span–Wagner equation of state contained some special “nonanalytical” terms in an attempt to reproduce the unusual fluid behavior very near the critical point. These terms also, however, caused unphysical oscillations in certain thermodynamic derivatives. One of the goals of this work was to construct an EOS without unphysical behavior while maintaining a good description of thermodynamic data near the critical point.

We begin by assessing the performance of the EOS for density in the critical region. Because the density becomes sensitive to small perturbations of temperature and pressure, it is common to evaluate density data in this region in terms of the deviation in pressure for a fixed temperature and density. We examine data at temperatures between 303 K and 307 K (near the critical temperature of 304.1282 K) and densities within 20 % of the critical density.

By far the most extensive study of densities in the critical region was the thesis of Tielkes [49] at the Ruhr University of Bochum, but the studies from Bochum of Duschek et al. [14, 35] and Nowak et al. [21] also have some points in the region considered, and a single set of measurements on the critical isotherm was reported by Straub [93]. In Table 6, we report the AARD and Bias from each of these sources. Because the density is very sensitive to temperature and pressure in this region, we report the AARD and Bias not in terms of density deviation as was the case in Sec. 4.7, but in terms of pressure as a function of temperature and density.

The Span–Wagner EOS better reproduces the single isotherm of Straub, but for the other studies, including the extensive data set from Tielkes, the new EOS has a lower AARD.

Table 6. Comparison for density data in the critical region. Statistics are based on relative deviations in pressure as a function of T and ρ

		This work		Span and Wagner	
First author	N	AARD (%)	Bias (%)	AARD (%)	Bias (%)
Duschek [14, 35]	31	0.0023	0.0013	0.0037	0.0004
Nowak [21]	22	0.0004	−0.0002	0.0028	−0.0024
Straub [93]	24	0.0039	0.0039	0.0003	0.0002
Tielkes [49]	1936	0.0014	0.0013	0.0026	−0.0020

The isochoric heat capacity c_v of CO_2 has been studied extensively in the critical region because its weak divergence provides a test for theories of critical scaling. Painstaking experiments were performed by Edwards [94]; these data were reanalyzed (with extra attention to the temperature scale) in conjunction with the work of Albright et al. [89]. The corrected data were not given in [89], but a tabulation was obtained from one of the authors of [89] and the tabulated data are available in [34].

In Fig. 23, we plot experimental data for c_v reported for densities at (or very near) the critical density. In addition to the data from Albright et al. [89], we include two studies [90, 91] that are generally consistent with these data. Two other studies [88, 92] are omitted for clarity; they are consistent with the others but show higher scatter. The plot also shows c_v calculated on the critical isochore from our new EOS and from the EOS of Span and Wagner. This figure is similar to Fig. 11 in [9].

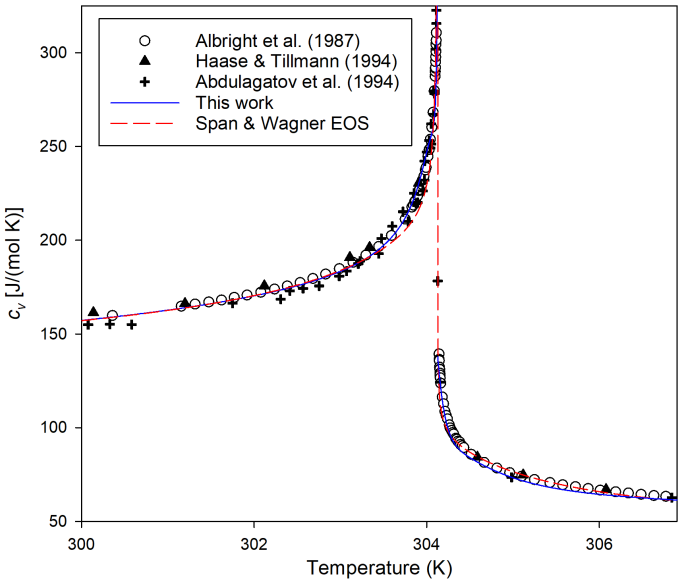

Fig. 23. Isochoric heat-capacity of CO_2 along the critical isochore from experiment and from equations of state. States on the left portion of the graph are in the two-phase region, with one-phase states in the right portion.

Both equations of state reproduce the experimental data very well. The new EOS is in slightly better agreement with data in the two-phase region (the portion of Fig. 23 to the left of the peak), while the Span–Wagner EOS is slightly better in the one-phase region (the right portion). The Span–Wagner EOS, with its special nonanalytical terms, is better able to describe the divergence in the one-phase region very close to the critical point (as evidenced by the peak in the red-dashed curve that the new EOS does not have), but the difference is only apparent in a tiny region within about 0.01 K of the critical temperature.

Additional near-critical data come from Kurzeja et al. [22], who reported the isothermal compressibility on an isochore near the critical density at temperatures slightly above the critical temperature. In Fig. 24, we plot these data (and also calculations from the Span–Wagner EOS) as the relative deviation from the new EOS. We limit the plot to data above 304.2 K, both because the critical point measured by Kurzeja et al. differed slightly from that used in the two EOS considered (see Sec. 2), which would distort comparisons very close to T_c, and because Kurzeja et al. observed that the isothermal compressibility in their experiments was distorted by gravity within approximately 55 mK of T_c. The new EOS is in very good agreement with these data, while the Span–Wagner EOS shows a systematic deviation within 0.5 K of T_c.

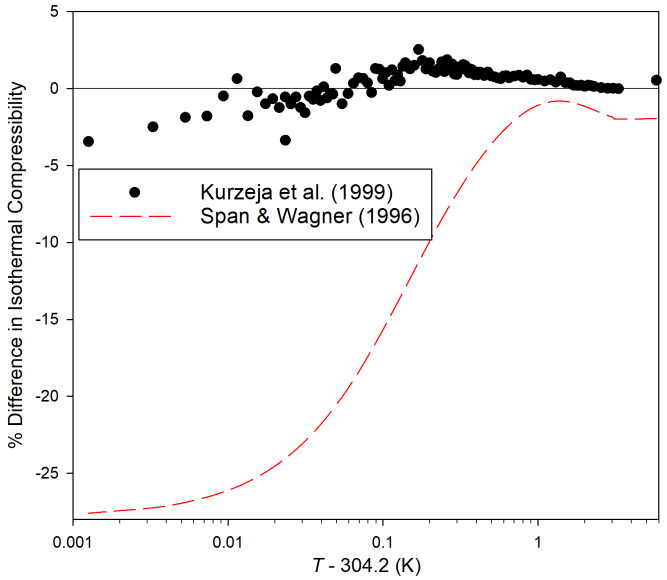

Fig. 24. Difference of experimental isothermal compressibility data [22] for CO_2 and calculations from the Span–Wagner EOS from the new EOS at a density of 468.511 kg m^{-3}.

One of the motivations for the new EOS was to remove some unphysical behavior that exists in the EOS of Span and Wagner for some derivative properties near the critical point; we will demonstrate two such cases here.

The first is the behavior of the isobaric heat capacity c_p at temperatures slightly above T_c. Figure 25 (which parallels Fig. 15 in [9]) shows c_p as a function of density for a temperature 0.1 K above the critical temperature. The Span–Wagner EOS has an unphysical depression in the function, while our new EOS correctly has a smooth peak.

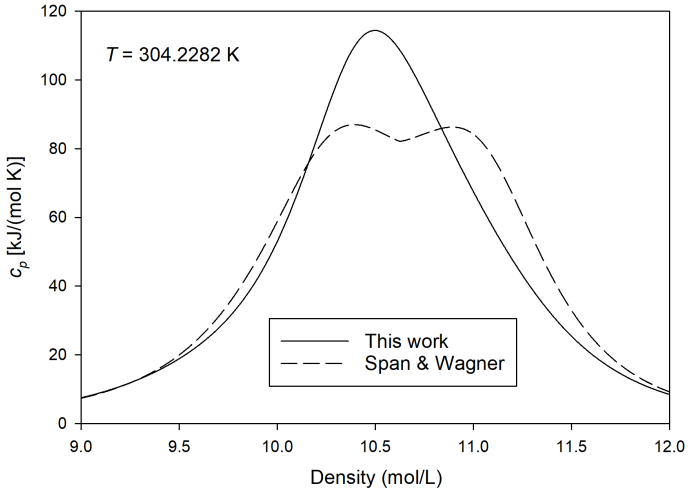

Fig. 25. Behavior of the isobaric heat capacity as a function of density for an isotherm 0.1 K above the critical temperature.

The heat capacity is a (second) temperature derivative of the thermodynamic potential, but a very similar situation exists with the isothermal compressibility κ_T, defined by

$$\kappa_T = -\frac{1}{v}\left(\frac{\partial v}{\partial p}\right)_T, \tag{11}$$

where $v = 1/\rho$ is the molar volume. This property depends on the first and second density derivatives of the thermodynamic potential.

Figure 26 shows the isothermal compressibility at a supercritical isotherm, 304.3 K. The behavior is very similar to that for c_p; the EOS of Span and Wagner displays unphysical behavior at densities within roughly 10 % of the critical density, while the EOS developed in this work correctly produces a smooth peak.

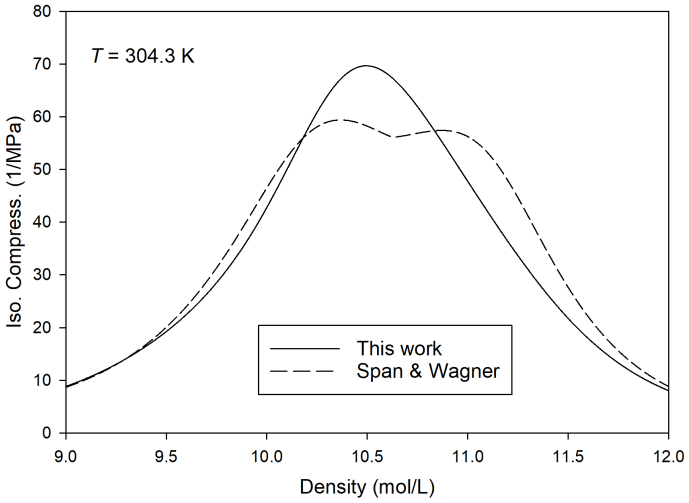

Fig. 26. Behavior of the isothermal compressibility as a function of density for a supercritical isotherm at 304.3 K.

It was noted by Huber et al. [11] that these unphysical behaviors of the Span–Wagner EOS distort calculations of the thermal conductivity near the critical point, because the enhancement of the thermal conductivity in the extended critical region depends on both c_p and κ_T. The new EOS eliminates that problem.

6. Range of Validity and Extrapolation

The range of validity of the equation of state is the stable fluid region up to a temperature of 2000 K and a pressure of 1000 MPa. At pressures above the triple-point pressure of 0.517 95 MPa, the lower temperature limit is the melting curve, which begins at the triple-point temperature of 216.5909 K [15] and goes to higher temperatures with increasing pressure; the melting curve is described in Sec. 10.1. Below the triple-point pressure, the boundary is the sublimation curve, which is described in Sec. 10.2.

We note that there are few experimental data above 800 K and above 150 MPa, so the properties computed from the EOS are more uncertain in those regions as described further in Sec. 8.

Physically reasonable extrapolation behavior of an equation of state is important. This is not only because some people might wish to model states beyond the official range of validity, but also because in mixture calculations the EOS may be called at conditions somewhat outside the range in which it was fitted. If the extrapolation is not physically reasonable, mixture calculations may fail or produce unreasonable results.

There are a few experimental data at extreme conditions that can provide a test of extrapolation. Datchi et al. [95] performed x-ray diffraction experiments in a diamond-anvil

cell at 709 K and reported densities (with relatively large uncertainties) up to 10 GPa. The densities were only shown graphically, but we obtained the numerical data from the authors and they are tabulated in [34]. Figure 27 shows that, while the two EOS extrapolate somewhat differently, both are generally consistent with these data within the scatter and uncertainty of the experiments.

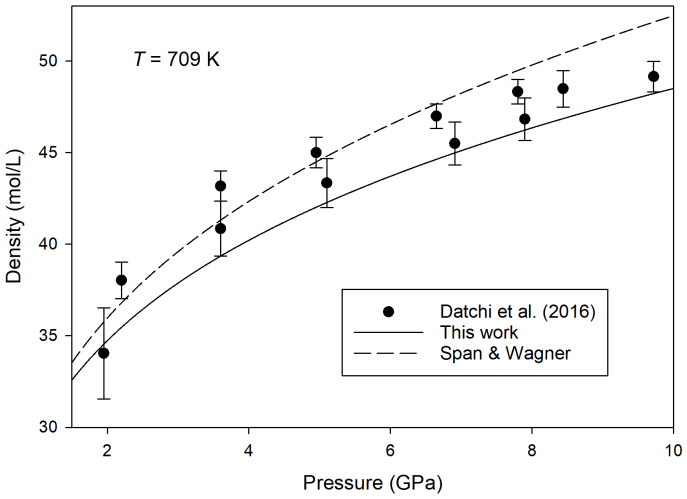

Fig. 27. Comparison of EOS extrapolation to high pressure for diamond-anvil cell density data of Datchi et al. [95] at 709 K.

Giordano et al. [96] reported Brillouin scattering measurements in a diamond-anvil cell up to 700 K and 8 GPa. These experiments produced a quantity that can, with assumptions about relaxation processes explained in [96], be related to the thermodynamic sound speed. The numerical data were obtained from the authors and tabulated in [34]. Both because the experiments are at extreme conditions and because the procedure for converting the measured quantity to thermodynamic sound speed relies on approximate assumptions, the resulting sound speeds have significant uncertainty, especially at higher pressures, perhaps on the order of 5–10 %.

In Fig. 28, we plot the thermodynamic sound speed for the 700 K isotherm along with calculations from both the new EOS and the Span–Wagner EOS. Both EOS agree with the data well at lower pressures and extrapolate to higher pressures in a physically reasonable manner, but at very high pressures (above the 1 GPa maximum valid pressure for the new EOS) the extrapolation of the new EOS is inferior to that of the Span–Wagner EOS. This is also true for the 500 K and 600 K isotherms from [96], and to a lesser extent for the 400 K and 300 K isotherms. This is a shortcoming that should be addressed in the development of a future reference EOS for CO_2. In the meantime, use of the Span–Wagner EOS may be preferred for geological and planetary applications at pressures above 1 GPa.

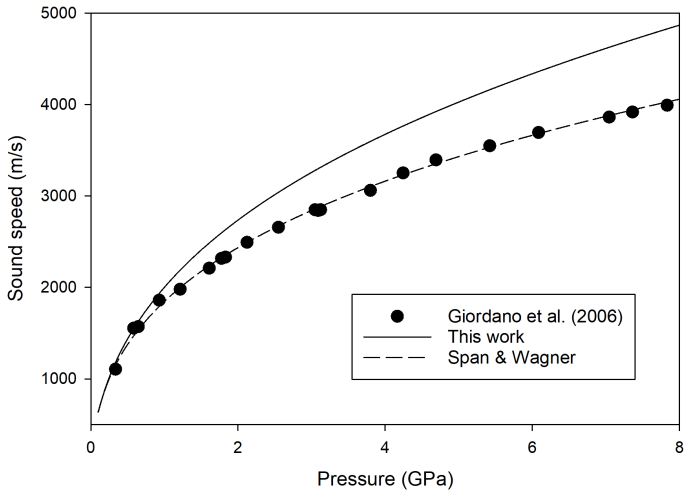

Fig. 28. Comparison of EOS extrapolation to high pressure for diamond-anvil sound-speed data of Giordano et al. [96] at 700 K.

The characteristic curves (sometimes called "ideal curves") are one indicator of the physical behavior, including extrapolation behavior, of an equation of state. The following curves are defined based on the compressibility factor $Z \equiv p/\rho RT$:

$$Z = 1, \tag{12}$$

$$\left(\frac{\partial Z}{\partial \rho}\right)_T = 0, \tag{13}$$

$$\left(\frac{\partial Z}{\partial T}\right)_p = 0, \tag{14}$$

$$\left(\frac{\partial Z}{\partial T}\right)_\rho = 0, \tag{15}$$

Equation (12) is called the ideal curve, Eq. (13) is called the Boyle curve, Eq. (14) is called the Joule–Thomson inversion curve, and Eq. (15) is called the Joule inversion curve.

For a well-behaved equation of state, these curves should be smooth and continuous, both within the range of validity and when extrapolated outside it. Figure 29 shows their behavior for the new EOS and for that of Span and Wagner. Both EOS perform well for the most part, although the new EOS provides smoother behavior of the Joule inversion curve at high pressures and low temperatures (this is far into the region where the equilibrium phase would be a solid, but it could conceivably be accessed in mixture calculations).

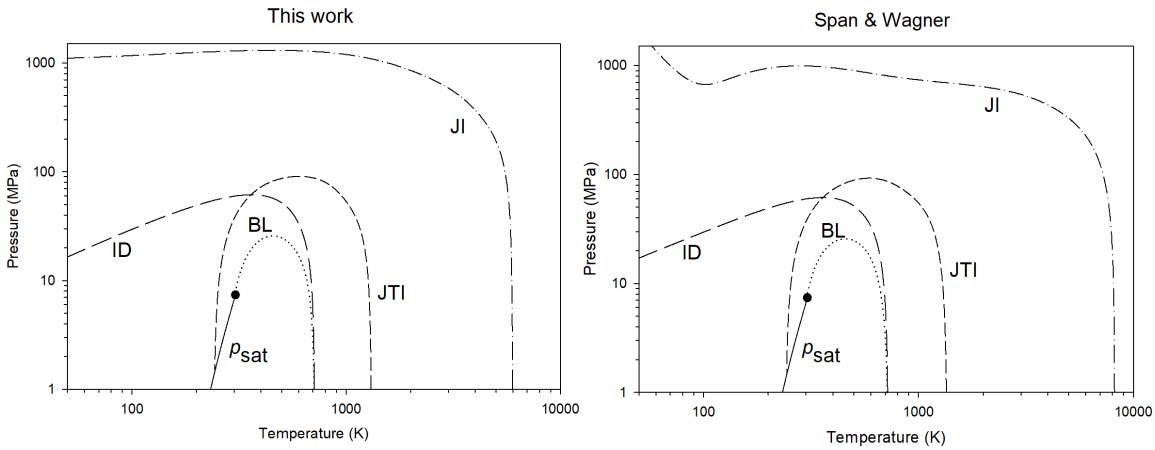

Fig. 29. Characteristic curves for this work and for the Span–Wagner EOS: Ideal curve (ID, dashed curve); Boyle curve (dotted curve, BL); Joule–Thomson inversion curve (short-dashed curve, JTI); Joule inversion curve (dash-dot curve, JI). The solid curve marked p_{sat} is the vapor-pressure curve, ending in the critical point which is a solid circle.

7. Auxiliary Functions

While the equation of state provides a complete account of the thermodynamics, for computational purposes (including initial guesses in iterative procedures) it is convenient to have simpler equations for certain quantities that are only functions of temperature. In this section, we provide such auxiliary functions, which closely reproduce calculations from the full EOS, for the saturated vapor pressure and for the saturated vapor and liquid densities.

Because the differences along the saturation boundary are small between our EOS and that of Span and Wagner [9], we adopt the same functional forms they used for their auxiliary equations. Only small adjustments to the coefficients (in addition to the small changes in critical density and critical pressure between the two EOS) are needed to fit the results computed from our EOS.

For the vapor pressure $p_{\mathrm{s}}(T)$, the auxiliary equation is

$$\ln\left(\frac{p_{\mathrm{s}}(T)}{p_{\mathrm{c}}}\right) = \frac{T_{\mathrm{c}}}{T}\left[\sum_{i=1}^{4} a_i \left(1-\frac{T}{T_{\mathrm{c}}}\right)^{t_i}\right], \tag{16}$$

with a_1 = −7.059 904, a_2 = 1.939 133, a_3 = −1.646 356, a_4 = −3.299 563, t_1 = 1, t_2 = 1.5, t_3 = 2, and t_4 = 4.

For the saturated liquid density $\rho_{\mathrm{L}}(T)$, the auxiliary equation is

$$\ln\left(\frac{\rho_{\mathrm{L}}(T)}{\rho_{\mathrm{c}}}\right) = \sum_{i=1}^{4} a_i \left(1-\frac{T}{T_{\mathrm{c}}}\right)^{t_i}, \tag{17}$$

with a_1 = 1.929 233, a_2 = −0.630 916, a_3 = −0.324 714, a_4 = 0.396 134, t_1 = 0.34, t_2 = 0.5, t_3 = 10/6, and t_4 = 11/6.

For the saturated vapor density $\rho_V(T)$, the auxiliary equation is

$$\ln\left(\frac{\rho_V(T)}{\rho_c}\right) = \sum_{i=1}^{5} a_i \left(1 - \frac{T}{T_c}\right)^{t_i}, \tag{18}$$

with a_1 = −1.696 815, a_2 = −0.845 878, a_3 = −4.577 673, a_4 = −10.130 93, a_5 = −29.7956, t_1 = 0.34, t_2 = 0.5, t_3 = 1, t_4 = 7/3, and t_5 = 14/3.

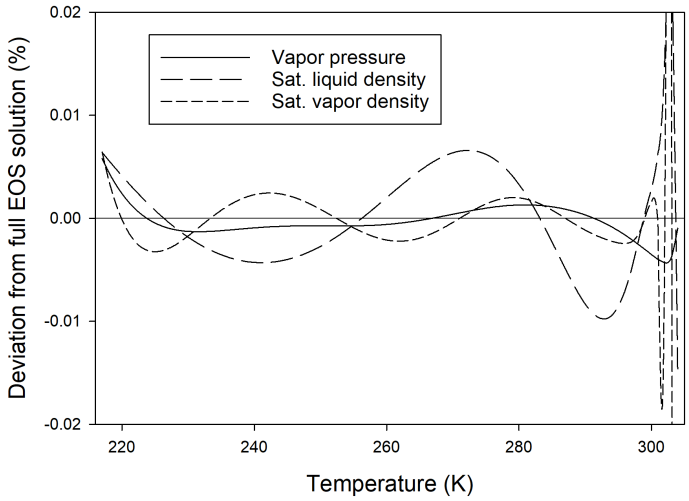

Fig. 30. Deviations of auxiliary equations for vapor pressure [Eq. (16)], saturated liquid density [Eq. (17)], and saturated vapor density [Eq. (18)] from the values computed rigorously from the equation of state.

Figure 30 shows the deviations of these auxiliary functions from the values obtained from the complete solution of the phase-equilibrium conditions for the equation of state. The deviations for the vapor pressure [Eq. (16)] are quite small, within 0.004 %. For the saturated liquid [Eq. (17)] and vapor [Eq. (18)] densities, deviations are within 0.01 % except very near the critical point.

8. Uncertainty

Span and Wagner [9] described the uncertainty of their equation of state for various properties in terms of a “tolerance” based on the fit to experimental data and the uncertainty of the underlying data. While they did not assign a definite meaning to this, we believe it is reasonable to interpret these as expanded uncertainties with coverage factor k = 2, comparable to a 95 % confidence interval.

As is evident from the comparisons in Sec. 4, for most properties at most conditions within the range of validity the reproduction of data is very similar between our EOS and the Span–Wagner EOS.

For the expanded (k = 2) relative uncertainty in vapor pressure, we estimate 0.01 % based on Fig. 5; Span and Wagner estimated 0.012 %. For the saturated liquid density, we adopt the estimates of Span and Wagner for the expanded uncertainty of 0.015 % below 295 K, 0.05 % between 295 K and 303 K, and 1 % between 303 K and T_c. For the saturated vapor density, we adopt the Span–Wagner estimates of 0.025 % below 295 K, 0.08 % between 295 K and 303 K, and 1 % between 303 K and T_c.

For density in the single-phase region, the uncertainties given in Fig. 38 of [9] are applicable to the new EOS as well. Similarly, we would not advocate changing the uncertainties for isobaric heat capacity expressed in Fig. 40 of [9].

For the sound speed, new experimental data described in Sec. 4.6 allow us to reduce the estimated uncertainty in some regions compared to that shown in Fig. 39 of [9]. For that paper's Region B (vapor between roughly 1 MPa and 5 MPa, up to 473 K), we reduce the estimate of the expanded (k = 2) uncertainty from 0.25 % to 0.05 %. For Region C (vapor up to 473 K between roughly 5 MPa and 10 MPa), we reduce the estimate from 0.5 % to 0.05 %. For liquid and dense supercritical states (Regions D and E) whose uncertainties in [9] ranged from 0.5 % to 2 %, we estimate 0.5 % at pressures up to 200 MPa at temperatures up to 400 K.

For all of these single-phase properties, we note that the uncertainties at the low-pressure end of the gas-phase portion of Figs. 38-40 in [9] become somewhat smaller than those shown in that paper, because the behavior approaches that of an ideal gas with uncertainty approaching zero (or approaching the uncertainty of c_p° for the isobaric heat capacity).

9. Computational Speed

The computational speed of an equation of state depends on both the number of terms in the formulation and on the types of terms; these factors may contribute differently depending on the computer and compiler used and on details on the implementation in computer code.

The EOS developed here has 24 terms (excluding the ideal-gas part), while that of Span and Wagner has 42 terms, three of which are so-called "nonanalytic" terms with a complicated functional form. While we have not performed comprehensive timing analysis, our limited testing indicates that, when used in the REFPROP software [10], the new EOS is faster to evaluate than the Span–Wagner EOS by factors of 1.5 to 2.

10. Melting and Sublimation Curves

The stable fluid region described by the equation of state is bounded at low temperatures by the melting and sublimation curves. Span and Wagner [9] provided empirical equations for these curves fitted to experimental data. Trusler [97] developed a model for the Gibbs energy for the solid and solved for the phase-equilibrium condition with the fluid EOS of Span and Wagner. Melting and sublimation data provided input for Trusler's solid EOS, so it is coupled both to the input data used and to the Span–Wagner EOS.

While both the Span–Wagner and Trusler formulations for the melting and sublimation curves provide reasonable descriptions, their use with the new EOS would not be seamless because they use a slightly different triple-point temperature. While our triple-point pressure of 0.517 95 MPa matches what was used previously, our triple-point temperature of 216.5909 K (from the metrological measurement in [15]) differs slightly from the 216.592 K used previously. This means that direct use of the existing formulations would cause a small discontinuity in the phase diagram. Instead of attempting to patch one of the older formulations, we have chosen to develop new melting and sublimation correlations.

One reason for developing new correlations is that we wish to impose thermodynamic consistency with other phase-change data by means of the Clapeyron equation. The Clapeyron equation relates the slope of the phase-transition boundary $\mathrm{d}p_{\mathrm{tr}}/\mathrm{d}T$ to the enthalpy and volume changes of the transition:

$$\frac{\mathrm{d}p_{\mathrm{tr}}}{\mathrm{d}T} = \frac{\Delta h_{\mathrm{tr}}}{T\Delta v_{\mathrm{tr}}}, \tag{19}$$

where Δh_{tr} and Δv_{tr} are the changes in molar enthalpy and molar volume for the melting or sublimation transition. The initial slope at the triple point is important when using triple-point cells in precision thermometry (where CO_2 is being studied as a replacement for the current ITS-90 mercury fixed point [15, 98, 99]), and consideration of the initial Clapeyron slope has been used to improve the correlation of the melting curve of SF_6 [100]. Some information about Δh_{tr} and Δv_{tr} was used to inform the solid EOS of Trusler [97], but we are able to include additional information, including a high-accuracy measurement of the enthalpy of melting Δh_{m} at the triple point [101] that the previous workers were apparently unaware of.

10.1. Melting Curve

There are a number of experimental data sources for the melting curve of carbon dioxide; some of them require special handling in order to convert their reported temperatures and/or pressures to modern scales.

The pioneering work of Bridgman [102] extended to approximately 1200 MPa and 367 K. However, it has been recognized since at least the 1960s [103] that the calibration of Bridgman's pressure gauge was slightly in error. He used a one-point calibration based on

the freezing pressure of mercury at 0 °C, which he took (in his units) to be 7640 kg_f/cm^2 (749.23 MPa). The best current value for this reference pressure is 756.84 MPa [104]. As recommended by Babb [103], we therefore multiply the pressures of Bridgman [102] by the ratio of these two pressures, which is 1.0102.

Michels et al. [105] studied the melting curve up to roughly 290 MPa (266 K), including some points near the triple point. However, care must be taken with the temperatures they reported, which were not on a standard scale. Span and Wagner [9] applied a constant offset to these temperatures to account for the different value assumed for the triple-point temperature of CO_2, but this simple adjustment can be improved. Michels et al. calibrated their thermometer at multiple points; in the range of interest here this included not only the triple point of CO_2 but also the freezing point of mercury at standard atmospheric pressure and the triple point of water. This means that the offsets to ITS-90 are different at different temperatures. For the triple point of CO_2, Michels et al. [105] used 216.58 K, which differs from the current value of 216.5909 K [15], requiring an adjustment to Michels' data of +0.011 K at that temperature. For the melting point of Hg, Michels et al. used 234.319 K [106] while the current recommendation is 234.3210 K [107], for an offset of +0.002 K. At the triple point of water (273.16 K), the offset is zero. We therefore applied an adjustment to the temperatures of Michels et al. obtained by linear interpolation between whichever two of these points bracketed the reported temperature.

Clusius et al. [108] reported points on the melting curve at pressures up to 24 MPa. Their temperature scale was based on a literature vapor-pressure equation for propane. Rather than reconstruct that indirect measurement, we can take advantage of the fact that they reported a triple point for CO_2 of 216.60 K, compared to the current value of 216.5909 K. Since the temperature range covered by Clusius et al. is only 5 K, it is reasonable to apply the corresponding adjustment of −0.009 K to all of their temperatures.

Giordano et al. [96] measured the melting curve at high temperatures and pressures (up to 800 K and 11 GPa) in a diamond-anvil cell. Data were presented graphically in the paper, but the authors supplied numerical data to us. Additional diamond-anvil melting data, extending up to 681 K and 7 GPa, were supplied by Abramson; these correspond to results shown graphically in a 2017 paper [109] and to some earlier unpublished data [110]; both sets are tabulated in [34]. It should be noted that the measurement of pressure in diamond-anvil cells is indirect, relying on the pressure dependence of optical properties of substances placed in the cell such as ruby or boron nitride, and it is not uncommon for different laboratories to differ somewhat in their pressure scales.

The slope $\mathrm{d}p_\mathrm{m}/\mathrm{d}T$ at the triple point can be obtained from the enthalpy of melting at the triple point reported by Ancsin [101] in the context of studies of CO_2 triple-point cells. A value of 200 J g^{-1} (8802 J mol^{-1}) was obtained. For the volume change of melting, Krupskii et al. [111] gave a solid molar volume at the triple point of 28.56 cm^3 mol^{-1}, obtained by extrapolation of x-ray diffraction experiments conducted up to 200 K. For the liquid molar

volume, our equation of state gives 37.345 cm^3 mol^{-1}, for a volume change on melting Δv_m = 8.785 cm^3 mol^{-1}. From Eq. (19), the initial Clapeyron slope is 4.63 MPa K^{-1}.

Significantly lower initial slopes are obtained if older data [112, 113] are used for Δh_m at the triple point; these values are inconsistent with the available data [105, 108] for the melting curve at low pressures. The same inconsistency was noted by Trusler [97], who used melting-curve data and the volumes of Krupskii et al. [111] to fit his equation of state for the solid and observed that the derived enthalpy of melting differed from literature values [112, 113] (Trusler was apparently unaware of the measurement of Ancsin [101], and cites another source [114] that only gives an indirect estimate of Δh_m rather than a measurement).

We should not arbitrarily dismiss the two older measurements of Δh_m, but in both cases there is evidence that the values are inaccurate. Maass and Barnes [112] reported Δh_m of 45.3 cal g^{-1} (8340 J mol^{-1}). In the same paper, they reported an enthalpy of sublimation at standard atmospheric pressure that agrees with other reliable data [115]. They used this enthalpy of sublimation, along with their enthalpy of melting and some small corrections, to obtain an enthalpy of vaporization of the liquid at the triple point of 88.1 cal g^{-1} (16 220 J mol^{-1}). However, this enthalpy of vaporization is accurately known from the EOS, and amounts to 15 425 J mol^{-1}, implying that the Δh_m from Maass and Barnes is too small. Eucken and Hauck [113] reported Δh_m of 1900.3 cal mol^{-1} (7950 J mol^{-1}), about 10 % lower than the value of Ancsin. In the same paper, they reported values of Δh_m that are also significantly low (on the order of 10 %) compared to more recent measurements for argon [116, 117] and ethene [118]. This strongly suggests a systematic error.

We are therefore justified in rejecting the two older data for Δh_m in favor of the value from Ancsin [101], which produces a Clapeyron slope of 4.63 MPa K^{-1} that is consistent with the experimental melting curve. However, because no uncertainty was given for Δh_m, we do not force the fit to have exactly that initial slope, but instead require it to be consistent within 1 %.

For the functional form of the melting equation, Trusler [97] found that the two-term expression used by Span and Wagner [9] was not able to reproduce melting data at pressures above 500 MPa. Trusler used a three-term expression of the form

$$p_\mathrm{m} = p_\mathrm{t}\left[1 + d_1\left(\frac{T}{T_\mathrm{t}} - 1\right) + d_2\left(\frac{T}{T_\mathrm{t}} - 1\right)^2 + d_3\left(\frac{T}{T_\mathrm{t}} - 1\right)^n\right], \tag{20}$$

with the exponent n on the last term set to 3. However, the initial slope of Trusler's correlation (which is $d_1 p_\mathrm{t}/T_\mathrm{t}$) is 4.81 MPa/K; this is inconsistent by roughly 4 % with the Clapeyron slope of 4.63 MPa/K obtained from Ancsin's careful measurement of Δh_m.

We fitted melting data to Eq. (20), finding better results with the exponent $n = 4$. Because of the larger uncertainty inherent to diamond-anvil experiments, we gave lower weight

to points from that method at pressures below 1200 MPa where data from more conventional experiments exist. We also excluded one point of Michels et al. [105] that was very close to the triple point and seemed to be an outlier. Our recommended melting-pressure equation is Eq. (20) with d_1 = 1950, d_2 = 1883.71, d_3 = 38.0324, and n = 4. This produces an initial slope $\mathrm{d}p_\mathrm{m}/\mathrm{d}T$ of 4.66 MPa/K, within 1 % of the value calculated from the Clapeyron equation.

In Fig. 31, we plot the percent deviation of the experimental data and of the two previous correlations from our melting-curve correlation, Eq. (20). The left panel shows the initial part of the curve, up to 240 K (where the pressure is near 120 MPa). The poor initial slope of the Trusler correlation is apparent; both our correlation and that of Span and Wagner give good results in this region. The right panel shows the entire range of data, corresponding to pressures up to roughly 11 GPa. Both our correlation and that of Trusler are able to describe the high-pressure data within their scatter, but the correlation of Span and Wagner is inadequate at these pressures.

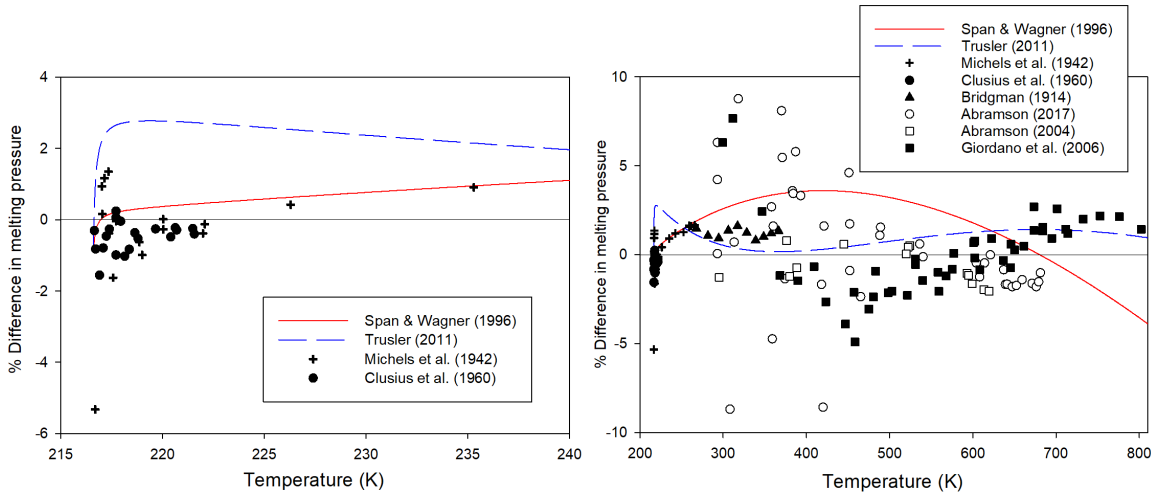

Fig. 31. Deviations of experimental data and of two previous correlations from our correlation for the melting curve, Eq. (20). Note the change in vertical scale between the two panels.

10.2. Sublimation Curve

For the sublimation curve, we can also obtain an initial slope at the triple point from the Clapeyron equation. The enthalpy of sublimation Δh_sub can be obtained by adding the melting enthalpy of Ancsin [101] to the enthalpy of vaporization at the triple point from the EOS; the result is 24 227 J mol^{-1}. Alternatively, we can take the enthalpy of sublimation at the normal sublimation point (p = 0.101 325 MPa) reported by Giauque and Egan [115] and correct it by adding the change in enthalpy of the saturated vapor from the normal sublimation point to the triple point (computed with our EOS) and subtracting the change

in enthalpy of the solid between those two points (computed from the solid equation of state of Trusler [97]). The result is 24 267 J mol^{-1}. The consistency of these two approaches (which would be perfect if Ancsin's Δh_{m} were 201 J g^{-1} instead of 200 J g^{-1}; the difference could be within the unstated uncertainty of Ancsin's result) reinforces our decision to adopt the melting enthalpy of Ancsin [101] in preference to older data. The volume change of sublimation at the triple point is computed using our equation of state for the vapor and the solid volume from Krupskii *et al.* [111]; Δv is 3169.9 cm^3 mol^{-1}. If we use the average of the two Δh_{sub} values derived above, the resulting $\mathrm{d}p_{\mathrm{sub}}/\mathrm{d}T$ is 0.0353 MPa K^{-1}. The sublimation-pressure equation proposed by Span and Wagner [9] is consistent with this Clapeyron slope, while the equation of Trusler [97] produces a slope about 1.5 % too large.

Data for sublimation pressures have been measured in several studies; some of the most precise work was around the normal sublimation point and those data have been carefully analyzed in the context of metrology. We require agreement within its uncertainty with the normal sublimation point recommended as a secondary reference point for temperature metrology by Bedford et al. [107], who give an ITS-90 temperature of 194.686 K with an uncertainty of 0.003 K at a sublimation pressure of 0.101 325 MPa. In previous work, the correlation of Span and Wagner [9] agreed with this point, but that of Trusler [97] produces a normal sublimation temperature of 194.673 K, well outside the uncertainty of that reference value.

We consider two experimental sources that Span and Wagner categorized as primary [119, 120] and one older study that they categorized as secondary [115]. In addition, Barber [121] performed precise measurements at pressures near 0.1 MPa. Baughman et al. [122] measured vapor pressures between approximately 201 K and 212 K in the context of mixture studies. Ancsin made precise metrological measurements between 170 K and 194.7 K that were presented in equation form in a report [123]; unfortunately, the underlying data were never published. We also consider the mass spectrometric data of Tickner and Lossing [124] because they cover low temperatures (106–154 K) where other data are lacking.

We do not include the sublimation pressures given in isotopic fractionation studies by Bilkaldi et al. [125] and Eiler et al. [126], the former of which were included in some previous work. In both of these studies, literature data for the vapor pressure of pure CO_2 with normal isotopic composition was used in some manner to calibrate the apparatus, meaning that the reported sublimation pressures do not represent independent data.

Like previous work [9, 97], we focus most of our attention on temperatures above 150 K. The low-temperature data of Tickner and Lossing [124] were included with a low weight in order to ensure reasonable extrapolation to those temperatures. We also gave lower weight to the older, more scattered data of Giauque and Egan [115] and to the data of Baughman et al. [122] that seemed to exhibit more scatter. We chose the same general functional form as has been used in previous work [9, 97], with somewhat different expo-

nents that were optimized by trial and error. The recommended correlation is

$$\ln\left(\frac{p_{\rm sub}}{p_{\rm t}}\right) = \left(\frac{T_{\rm t}}{T}\right)\left[d_4\left(1-\frac{T}{T_{\rm t}}\right) + d_5\left(1-\frac{T}{T_{\rm t}}\right)^{1.9} + d_6\left(1-\frac{T}{T_{\rm t}}\right)^{2.3}\right], \qquad (21)$$

with d_4 = −14.82, d_5 = 5.2016, and d_6 = −6.7287. This produces a slope at the triple point of 0.0354 MPa K^{-1} and a normal sublimation temperature of 194.6858 K.

Figure 32 compares Eq. (21) and the two older correlations to the experimental data. Our correlation is in very good agreement with the high-accuracy data sources that exist above 170 K [119–121, 123]. Notably, we agree with the recommended normal sublimation point, which the correlation of Trusler does not. The correlation of Span and Wagner also performs well in most of this region, although it appears to be deviating in the positive direction below 180 K.

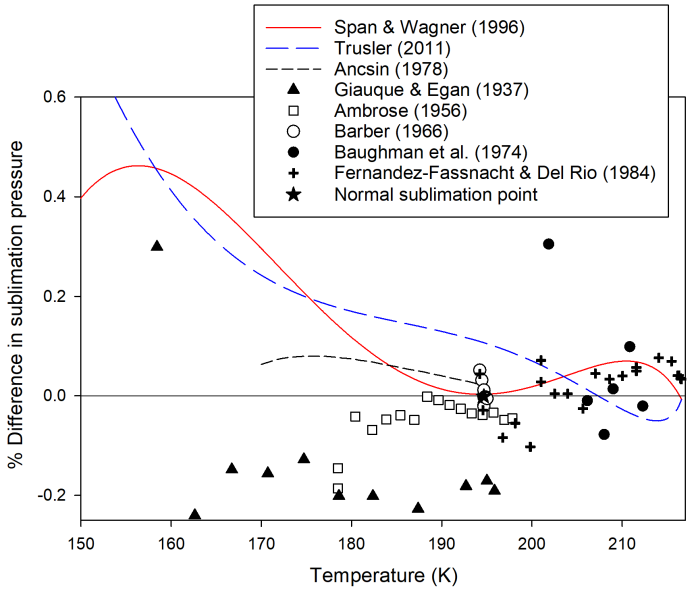

Fig. 32. Relative deviations of experimental data and of two previous correlations from our correlation for the sublimation curve, Eq. (21).

Not shown in Fig. 32 is the extrapolation to lower temperatures, where the available data are of much lower accuracy due to the very low pressures involved. Our differences from the data of Tickner and Lossing [124] are mostly on the order of 5 %, rising to 13 % below 110 K. Data from Bryson et al. [127], which were not used at all in our fit, cover roughly 70–100 K; they are generally reproduced within a factor of two, which is similar to their scatter.

11. Effect on Transport Property Reference Correlations

The equation of state affects the correlations for transport properties (viscosity and thermal conductivity) in two ways. First, the transport properties are modeled as a function of temperature and density, while experimental data are almost always reported as a function of temperature and pressure. This requires an EOS to determine the density of the experimental measurements, and use of a different EOS will produce different densities and therefore different values for the transport properties. Second, certain properties from the EOS, such as the isothermal compressibility, appear in the theory-based expressions used to model the enhancement of transport properties near the critical point. For the viscosity, this enhancement is negligible for most purposes, but it is significant in a fairly wide region of the parameter space for the thermal conductivity.

The current reference formulations for these properties are the correlation of Laesecke and Muzny [128] for the viscosity and that of Huber et al. [11] for the thermal conductivity. We used comprehensive databases of experimental transport property data and compared calculations of those properties that used both the Span–Wagner EOS and the new EOS. The differences were much smaller than the uncertainties in the formulations and in the experimental data.

As a result of this analysis, we conclude that the existing formulations [11, 128] can continue to be used, with their existing parameters, in conjunction with the EOS developed in this work to calculate the viscosity and thermal conductivity of carbon dioxide.

12. Conclusions and Outlook

We have developed an equation of state for carbon dioxide as an alternative to the existing reference EOS by Span and Wagner [9]. While the Span–Wagner EOS remains the default in NIST's REFPROP software [10], the new EOS can be used as an alternative by users who desire the greater computational speed and/or the other improvements noted below.

For most conditions of interest, both EOS produce very accurate results and neither performs significantly better than the other in its representation of measured data. The new EOS provides an improved ideal-gas heat capacity, which means that its gas-phase heat capacities should be more accurate. The second virial coefficient $B(T)$ is improved except in the range 250–350 K, and the third virial coefficient $C(T)$ is significantly improved. Data near the critical point for densities and heat capacities are represented well in spite of the lack of the special near-critical terms that were used in [9]. The new EOS provides some improvement for sound speeds at some conditions and for supercritical densities. The new EOS is free of the unphysical oscillations in derivative properties near the critical point that afflicted the Span–Wagner EOS.

The new EOS is faster than the Span–Wagner EOS by a factor of roughly 1.5–2 (within the framework of the NIST REFPROP software). This should be helpful for users who wish to perform highly iterative calculations.

There are some areas that should be improved or at least further examined in any future effort to produce a definitive reference EOS. There appears to be room for improvement in describing the vapor pressure between 220 K and 260 K. The description of sound speeds at pressures above 1 GPa seems to be poor as shown in Fig. 28 (although one cannot be certain since only one data set is available). The behavior of the EOS in mixture calculations was among the motivations for this work; while the use of more modern EOS technology with good extrapolation behavior should improve that aspect of the performance, we did not have the labor available to check it. Given the importance of mixtures with CO_2 in many applications, mixture behavior should play an important role when a final reference EOS is developed.

We reiterate that the previously developed formulations for viscosity [128] and thermal conductivity [11] can continue to be used in conjunction with the new equation of state.

Finally, we note that a Fluid file for use in NIST's REFPROP software has been made available in the NIST Public Data Repository [129]. This file contains the alternative EOS formulation developed here, along with the new melting and sublimation correlations and also all of the property formulations that were already available in REFPROP Version 10.0 [10].

References

[1] Dennis RA, Harp R (2007) Overview of the U.S. Department of Energy's Office of Fossil Energy Advanced Turbine Program for coal based power systems with carbon capture. *Proceedings of ASME Turbo Expo 2007* (ASME Press, New York), Vol. 2, pp 1093–1104.

[2] Allam R, Martin S, Forrest B, Fetvedt J, Lu X, Freed D, Brown Jr GW, Sasaki T, Itoh M, Manning J (2017) Demonstration of the Allam cycle: An update on the development status of a high efficiency supercritical carbon dioxide power process employing full carbon capture. *Energy Procedia* 114:5948–5966. https://doi.org/10.1016/j.egypro.2017.03.1731

[3] Brun K, Friedman P, Dennis R (eds) (2017) *Fundamentals and Applications of Supercritical Carbon Dioxide (sCO$_2$) Based Power Cycles* (Woodhead Publishing, Duxford, UK).

[4] Scaccabarozzi R, Gatti M, Martelli E (2016) Thermodynamic analysis and numerical optimization of the NET Power oxy-combustion cycle. *Appl Energy* 178:505–526. https://doi.org/10.1016/j.apenergy.2016.06.060

[5] White MT, Bianchi G, Chai L, Tassou SA, Sayma AI (2021) Review of supercritical CO_2 technologies and systems for power generation. *Appl Therm Eng* 185:116447. https://doi.org/10.1016/j.applthermaleng.2020.116447

[6] Zhao Q, Mecheri M, Neveux T, Privat R, Jaubert JN (2017) Selection of a proper equation of state for the modeling of a supercritical CO_2 Brayton cycle: Consequences on the process design. *Ind Eng Chem Res* 56:6841–6853. https://doi.org/10.1021/acs.iecr.7b00917

[7] Li H, Dong B, Yu Z, Yan J, Zhu K (2019) Thermo-physical properties of CO_2 mixtures and their impacts on CO_2 capture, transport and storage: Progress since 2011. *Appl Energy* 255:113789. https://doi.org/10.1016/j.apenergy.2019.113789

[8] Rasmussen E, Yellapantula S, Martin MJ (2021) How equation of state selection impacts accuracy near the critical point: Forced convection supercritical CO_2 flow over a cylinder. *J Supercrit Fluids* 171:105141. https://doi.org/10.1016/j.supflu.2020.105141

[9] Span R, Wagner W (1996) A new equation of state for carbon dioxide covering the fluid region from the triple-point temperature to 1100 K at pressures up to 800 MPa. *J Phys Chem Ref Data* 25:1509–1596. https://doi.org/10.1063/1.555991

[10] Lemmon EW, Bell IH, Huber ML, McLinden MO (2018) NIST Standard Reference Database 23: Reference Fluid Thermodynamic and Transport Properties-REFPROP, Version 10.0, National Institute of Standards and Technology. https://doi.org/10.18434/T4/1502528.

[11] Huber ML, Sykioti EA, Assael MJ, Perkins RA (2016) Reference correlation of the thermal conductivity of carbon dioxide from the triple point to 1100 K and up to 200 MPa. *J Phys Chem Ref Data* 45:013102. https://doi.org/10.1063/1.4940892

[12] Wieser ME, Berglund M (2009) Atomic weights of the elements 2007 (IUPAC Technical Report). *Pure Appl Chem* 81:2131–2156. https://doi.org/doi:10.1351/PAC-REP-09-08-03
[13] Mohr PJ, Newell DB, Taylor BN, Tiesinga E (2025) CODATA recommended values of the fundamental physical constants: 2022. *J Phys Chem Ref Data* 54:033105. https://doi.org/10.1063/5.0279860
[14] Duschek W, Kleinrahm R, Wagner W (1990) Measurement and correlation of the (pressure, density, temperature) relation of carbon dioxide II. Saturated-liquid and saturated-vapour densities and the vapour pressure along the entire coexistence curve. *J Chem Thermodyn* 22:841–864. https://doi.org/10.1016/0021-9614(90)90173-N
[15] Kawamura Y, Matsumoto N, Nakano T (2020) Realization of the triple point of carbon dioxide evaluated by the ITS-90. *Metrologia* 57:015004. https://doi.org/10.1088/1681-7575/ab451e
[16] Preston-Thomas H (1990) The International Temperature Scale of 1990 (ITS-90). *Metrologia* 27:3–10. https://doi.org/10.1088/0026-1394/27/1/002. ; Erratum, **27**, 107
[17] Rusby RL (1991) The conversion of thermal reference values to the ITS-90. *J Chem Thermodyn* 23:1153–1161. https://doi.org/10.1016/S0021-9614(05)80148-X
[18] Moldover MR (1974) Visual observation of the critical temperature and density: CO_2 and C_2H_4. *J Chem Phys* 61:1766–1778. https://doi.org/10.1063/1.1682173
[19] Moldover MR, Sengers JV, Gammon RW, Hocken RJ (1979) Gravity effects in fluids near the gas-liquid critical point. *Rev Mod Phys* 51:79–99. https://doi.org/10.1103/RevModPhys.51.79
[20] Abdulagatov IM, Polikhronidi NG, Batyrova RG (1994) Isochoric heat capacity and liquid-gas coexistence curve of carbon dioxide in the region of the immediate vicinity of the critical point. *Ber Bunsenges Phys Chem* 98:1068–1072. https://doi.org/10.1002/bbpc.19940980812
[21] Nowak P, Tielkes T, Kleinrahm R, Wagner W (1997) Supplementary measurements of the (p,ρ,T) relation of carbon dioxide in the homogeneous region at T = 313 K and on the coexistence curve at T = 304 K. *J Chem Thermodyn* 29:885–889. https://doi.org/10.1006/jcht.1997.0208
[22] Kurzeja N, Tielkes T, Wagner W (1999) The nearly classical behavior of a pure fluid on the critical isochore very near the critical point under the influence of gravity. *Int J Thermophys* 20:531–561. https://doi.org/10.1023/A:1022657121329
[23] Head DI, Hermier Y, Rusby RL, Bonnier G, Wei M (1990) Measurements of carbon dioxide and xenon triple point cells. *Proceedings, TEMPMEKO 90: 4th Symposium on Temperature and Thermal Measurement in Industry and Science* (Helsinki, Finland), pp 118–125.
[24] Pavese F, Ferri D (1982) Ten years of research on sealed cells for phase transition studies of gases at IMGC. *Temperature: Its Measurement in Science and Industry* (American Institute of Physics), Vol. 5, pp 217–227.

[25] Span R (2000) *Multiparameter Equations of State: An Accurate Source of Thermodynamic Property Data* (Springer, Berlin).
[26] Tashkun SA, Harvey AH (2021) Ideal-gas thermochemical properties for carbon dioxide and its isotopologues calculated from partition functions, National Institute of Standards and Technology. https://doi.org/10.18434/mds2-2364.
[27] Tashkun SA, Harvey AH (2025) Partition functions and ideal-gas thermodynamics for carbon dioxide. *J Phys Chem Ref Data* 54:023102. https://doi.org/10.1063/5.0276615
[28] Fischer J, de Podesta M, Hill KD, Moldover M, Pitre L, Rusby R, Steur P, Tamura O, White R, Wolber L (2011) Present estimates of the differences between thermodynamic temperatures and the ITS-90. *Int J Thermophys* 32:12–25. https://doi.org/10.1007/s10765-011-0922-1
[29] Gaiser C, Fellmuth B, Gavioso RM, Kalemci M, Kytin V, Nakano T, Pokhodun A, Rourke PMC, Rusby R, Sparasci F, Steur PPM, Tew WL, Underwood R, White R, Yang I, Zhang J (2022) 2022 update for the differences between thermodynamic temperature and ITS-90 below 335 K. *J Phys Chem Ref Data* 51:043105. https://doi.org/10.1063/5.0131026
[30] Lemmon EW, Jacobsen RT (2005) A new functional form and new fitting techniques for equations of state with application to pentafluoroethane (HFC-125). *J Phys Chem Ref Data* 34:69–108. https://doi.org/10.1063/1.1797813
[31] Akasaka R, Lemmon EW (2025) A Helmholtz energy equation of state for 3,3,3-trifluoroprop-1-ene (R-1243zf). *Int J Thermophys* 46:23. https://doi.org/10.1007/s10765-024-03481-6
[32] Harvey AH (2021) What the thermophysical property community should know about temperature scales. *Int J Thermophys* 42:165. https://doi.org/10.1007/s10765-021-02915-9
[33] Hellmann R (2014) Ab initio potential energy surface for the carbon dioxide molecule pair and thermophysical properties of dilute carbon dioxide gas. *Chem Phys Lett* 613:133–138. https://doi.org/10.1016/j.cplett.2014.08.057
[34] Harvey AH (2022) Thermodynamic data from unpublished sources to support the new reference equation of state for carbon dioxide, National Institute of Standards and Technology. https://doi.org/10.18434/mds2-2721.
[35] Duschek W, Kleinrahm R, Wagner W (1990) Measurement and correlation of the (pressure, density, temperature) relation of carbon dioxide I. The homogeneous gas and liquid regions in the temperature range from 217 K to 340 K at pressures up to 9 MPa. *J Chem Thermodyn* 22:827–840. https://doi.org/10.1016/0021-9614(90)90172-M
[36] Mantilla ID, Cristancho DE, Ejaz S, Hall KR, Atilhan M, Iglesias-Silva GA (2010) $p-\rho-t$ data for carbon dioxide from (310 to 450) K up to 160 MPa. *J Chem Eng Data* 55:4611–4613. https://doi.org/10.1021/je1001158
[37] Duarte CMM, Menduiña C, Aguiar-Ricardo A, Nunes da Ponte M (2002) Second and third virial coefficients of three binary mixtures containing xenon, at 273 K: Compari-

son between Xe + C_2H_6, Xe + C_2H_4 and Xe + CO_2. *Phys Chem Chem Phys* 4:4709–4715. https://doi.org/10.1039/B203040C

[38] Feng XJ, Liu Q, Zhou MX, Duan YY (2010) Gaseous $pvTx$ properties of mixtures of carbon dioxide and propane with the Burnett isochoric method. *J Chem Eng Data* 55:3400–3409. https://doi.org/10.1021/je100148h

[39] Glowka S (1990) Determination of volumetric properties of ammonia between 298 and 473 K and carbon dioxide between 304 and 423 K using the Burnett method. *Pol J Chem* 64:699–709.

[40] Holste JC, Hall KR, Eubank PT, Esper G, Watson MQ, Warowny W, Bailey DM, Young JG, Bellomy MT (1987) Experimental (p, V_m, T) for pure CO_2 between 220 and 450 K. *J Chem Thermodyn* 19:1233–1250. https://doi.org/10.1016/0021-9614(87)90001-2

[41] Patel MR, Joffrion LL, Eubank PT (1988) A simple procedure for estimating virial coefficients from Burnett PVT data. *AIChE J* 34:1229–1232. https://doi.org/10.1002/aic.690340722

[42] Waxman M, Davis HA, Hastings JR (1973) A new determination of the second virial coefficient of carbon dioxide at temperatures between 0° and 150°C, and an evaluation of its reliability. *Proceedings of the Sixth Symposium on Thermophysical Properties* (ASME, New York), pp 245–255.

[43] Hellmann R (2017) Nonadditive three-body potential and third to eighth virial coefficients of carbon dioxide. *J Chem Phys* 146:054302. https://doi.org/10.1063/1.4974995

[44] Bignell N, Bean VE (1988) A fixed point on the pressure scale: Carbon dioxide vapor pressure at 273.16 K. *Metrologia* 25:141–145. https://doi.org/10.1088/0026-1394/25/3/003

[45] Edwards JL, Johnson DP (1968) A dynamic method for determining the vapor pressure of carbon dioxide at 0 °C. *J Res Nat Bur Stand* 72C:27–32. https://doi.org/10.6028/jres.072C.003

[46] Kartal Dogan A, Bonnier G, Uytun A, Kocas I, Durgut Y (2011) Toward carbon dioxide vapor-pressure thermometer. *Int J Thermophys* 32:2230–2238. https://doi.org/10.1007/s10765-011-1091-y4

[47] Haynes WM (1986) Orthobaric liquid densities and dielectric constants of carbon dioxide. *Advances in Cryogenic Engineering: Volume 31*, ed Fast RW (Springer US, Boston, MA), pp 1199–1204. https://doi.org/10.1007/978-1-4613-2213-9_133

[48] Saleh B, Wendland M (2005) Measurement of vapor pressures and saturated liquid densities of pure fluids with a new apparatus. *J Chem Eng Data* 50:429–437. https://doi.org/10.1021/je0497496

[49] Tielkes T (1996) *Präzisionsmessungen der thermischen Zustandsgrössen im kritischen Gebiet von Kohlendioxid*. Ph.D. thesis. Ruhr-Universität Bochum, Bochum, Germany.

[50] Klimeck J, Kleinrahm R, Wagner W (2001) Measurements of the (p,ρ,T) relation of methane and carbon dioxide in the temperature range 240 K to 520 K at pressures

up to 30 MPa using a new accurate single-sinker densimeter. *J Chem Thermodyn* 33:251–267. https://doi.org/10.1006/jcht.2000.0711

[51] Gilgen R, Kleinrahm R, Wagner W (1992) Supplementary measurements of the (pressure, density, temperature) relation of carbon dioxide in the homogeneous region at temperatures from 220 K to 360 K and pressures up to 13 MPa. *J Chem Thermodyn* 24:1243–1250. https://doi.org/10.1016/S0021-9614(05)80264-2

[52] Jaeschke M (1987) Determining the compressibility factors of carbon dioxide from refractive index measurements. Personal communication from Ruhrgas AG, cited in Ref. 9.

[53] Jaeschke M (1987) Determining the compressibility factors of carbon dioxide from Burnett measurements. Personal communication from Ruhrgas AG, cited in Ref. 9.

[54] Fenghour A, Wakeham WA, Watson JTR (1995) Amount-of-substance density of CO_2 at temperatures from 329 K to 698 K and pressures up to 34 MPa. *J Chem Thermodyn* 27:219–223. https://doi.org/10.1006/jcht.1995.0019

[55] Hoinkis J (1989) *Untersuchung zum thermischen Verhalten von binären Gasmischen mit Kohlendioxid*. Ph.D. thesis. TH Karlsruhe, Karlsruhe, Germany.

[56] Kirillin VA, Ulybin SA, Zherdev EP (1969) Experimental investigation of carbon dioxide density at temperatures from -50 to +200°C and pressures to 500 bars. *Proc 1st Int Conf Calorimetry Thermodyn* 1:641–647.

[57] Gomez-Osorio MA, Browne RA, Carvajal Diaz M, Hall KR, Holste JC (2016) Density measurements for ethane, carbon dioxide, and methane + nitrogen mixtures from 300 to 470 K up to 137 MPa using a vibrating tube densimeter. *J Chem Eng Data* 61:2791–2798. https://doi.org/10.1021/acs.jced.6b00138

[58] Sanchez-Vicente Y, Tay WJ, Al Ghafri SZ, Trusler JPM (2018) Thermodynamics of carbon dioxide-hydrocarbon systems. *Appl Energy* 220:629–642. https://doi.org/10.1016/j.apenergy.2018.03.136

[59] Ihmels EC, Gmehling J (2001) Densities of toluene, carbon dioxide, carbonyl sulfide, and hydrogen sulfide over a wide temperature and pressure range in the sub- and supercritical state. *Ind Eng Chem Res* 40:4470–4477. https://doi.org/10.1021/ie001135g

[60] Mazzoccoli M, Bosio B, Arato E (2012) Pressure–density–temperature measurements of binary mixtures rich in CO_2 for pipeline transportation in the CCS process. *J Chem Eng Data* 57:2774–2783. https://doi.org/10.1021/je300590v

[61] Yang X, Richter M, Wang Z, Li Z (2015) Density measurements on binary mixtures (nitrogen+carbon dioxide and argon+carbon dioxide) at temperatures from (298.15 to 423.15) K with pressures from (11 to 31) MPa using a single-sinker densimeter. *J Chem Thermodyn* 91:17–29. https://doi.org/10.1016/j.jct.2015.07.014

[62] Brachthäuser K, Kleinrahm R, Lösch HW, Wagner W (1993) Entwicklung eines neuen dichte-meßverfahrens und aufbau einer hochtemperatur-hochdruck-dichtemeßanlage (Fortschritt-Berichte VDI, Reihe 8, Düsseldorf), 371.

[63] Vukalovich MP, Altunin VV (1959) Experimental investigation of the $p-v-t$ dependence of carbon dioxide. *Teploenergetika* 6(11):58–65.

[64] Vukalovich MP, Altunin VV, Timoshenko NI (1962) Experimental investigation of the specific volumes of CO_2 at temperatures 250–700°C and pressures up to 600 kg/cm^2. *Teploenergetika* 9(5):56–62.
[65] Vukalovich MP, Altunin VV, Timoshenko NI (1963) On investigating the compressibility of carbon dioxide at high temperatures. *Teploenergetika* 10(2):92–93.
[66] Shmonov VM, Shmulovich KI (1974) Molal volumes and equation of state of CO_2 at temperatures from 100 to 1000 °C and pressures from 2000 to 10,000 bars. *Dokl Akad Nauk SSSR* 217:935–938.
[67] Seitz JC, Blencoe JG, Bodnar RJ (1996) Volumetric properties for $(1-x)CO_2 + xCH_4$, $(1-x)CO_2 + xN_2$, and $(1-x)CH_4 + xN_2$ at the pressures (9.94, 19.94, 29.94, 39.94, 59.93, 79.93, and 99.93) MPa and temperatures (323.15, 373.15, 473.15, and 573.15) K. *J Chem Thermodyn* 28:521–538. https://doi.org/10.1006/jcht.1996.0049
[68] Novikov II, Trelin YS (1960) The velocity of sound along the vapor-liquid phase equilibrium curve. The velocity of sound propagation in saturated carbon dioxide vapors. *Zh Prikl Mekh Tekh Fiz* (2):112–115.
[69] Novikov II, Trelin YS (1962) A new method of calculation of the thermodynamic diagram of working fluids. *Teploenergetika* 9(2):79–85.
[70] Estrada-Alexanders AF, Trusler JPM (1998) Speed of sound in carbon dioxide at temperatures between (220 and 450) K and pressures up to 14 MPa. *J Chem Thermodyn* 30:1589–1601. https://doi.org/10.1006/jcht.1998.0428
[71] Estrada-Alexanders AF, Hurly JJ (2008) Kinematic viscosity and speed of sound in gaseous CO, CO_2, SiF_4, SF_6, C_4F_8, and NH_3 from 220 K to 375 K and pressures up to 3.4 MPa. *J Chem Thermodyn* 40:193–202. https://doi.org/10.1016/j.jct.2007.07.002
[72] Kanishchev BE, Pitaevskaya LL, Gutman SL (1981) Speed of sound in nitrogen, carbon dioxide, and mixtures thereof at high pressures. *Dokl Akad Nauk SSSR* 257:1348–1351.
[73] Lemming W (1989) Experimentelle Bestimmung Akustischer und Thermischer Virialkoeffizienten von Arbeits-stoffen der Energietechnik (Fortschritt-Berichte VDI, Reihe 19, Düsseldorf), No. 32.
[74] Lin CW, Trusler JPM (2014) Speed of sound in (carbon dioxide + propane) and derived sound speed of pure carbon dioxide at temperatures between (248 and 373) K and at pressures up to 200 MPa. *J, Chem, Eng, Data* 59:4099–4109. https://doi.org/10.1021/je5007407
[75] Liu Q, Feng X, An B, Duan Y (2014) Speed of sound measurements using a cylindrical resonator for gaseous carbon dioxide and propene. *J Chem Eng Data* 59:2788–2798. https://doi.org/10.1021/je500424b
[76] Pecceu W, Van Dael W (1973) Ultrasonic velocity in liquid carbon dioxide. *Physica* 63:154–162. https://doi.org/10.1016/0031-8914(73)90184-5
[77] Pitaevskaya LL, Bilevich AV (1973) The velocity of ultrasound in carbon dioxide at pressures up to 4.5 kbar. *Russ J Phys Chem* 47:126–127.
[78] Rivas C, Gimeno B, Artal M, Blanco ST, Fernández J, Velasco I (2016) High-pressure speed of sound in pure CO_2 and in CO_2 with SO_2 as an impurity using methanol as a

doping agent. *Int J Greenhouse Gas Control* 54:737–751. https://doi.org/10.1016/j.ijggc.2016.09.014

[79] Ernst G, Maurer G, Wiederuh E (1989) Flow calorimeter for the accurate determination of the isobaric heat capacity at high pressures; results for carbon dioxide. *J Chem Thermodyn* 21:53–65. https://doi.org/10.1016/0021-9614(89)90007-4

[80] Ernst G, Hochberg UE (1989) Flow-calorimetric results for the specific heat capacity c_p of CO_2, of C_2H_6, and of ($0.5CO_2$ + $0.5C_2H_6$) at high pressures. *J Chem Thermodyn* 21:407–414. https://doi.org/10.1016/0021-9614(89)90141-9

[81] Ishmael MPE, Lukawski MZ, Tester JW (2016) Isobaric heat capacity (C_p) measurements of supercritical fluids using flow calorimetry: equipment design and experimental validation with carbon dioxide, methanol, and carbon dioxide-methanol mixtures. *J Supercrit Fluids* 117:72–79. https://doi.org/10.1016/j.supflu.2016.05.016

[82] Dordain L, Coxam JY, Quint JR, Grolier JPE, Lemmon EW, Penoncello SG (1995) Isobaric heat capacities of carbon dioxide and argon between 323 and 423 K and at pressures up to 25 MPa. *J Supercrit Fluids* 8:228–235. https://doi.org/10.1016/0896-8446(95)90035-7

[83] Rivkin SL, Gukov VM (1969) Experimental study of the isobaric specific heat of carbon dioxide at supercritical pressures. *Teploenergetika* 15(10):72–75.

[84] Vukalovich MP, Altunin VV, Gureev AN (1965) Experimental study of the thermal capacity c_p of carbon dioxide at high pressures. *Teploenergetika* 12(7):58–62.

[85] Amirkhanov KI, Polikhronidi NG, Batyrova RG (1970) Experimental determination of specific heat c_v of carbon dioxide. *Thermal Eng* 17(3):101–104.

[86] Amirkhanov KI, Polikhronidi NG, Alibekov BG, Batyrova RG (1971) Isochoric specific heat-capacity of carbon dioxide. *Thermal Eng* 18(12):87–91.

[87] Magee JW, Ely JF (1986) Specific heats (C_v) of saturated and compressed liquid and vapor carbon dioxide. *Int J Thermophys* 7:1163–1182. https://doi.org/10.1007/BF00503973

[88] Beck L, Ernst G, Gürtner J (2002) Isochoric heat capacity c_v of carbon dioxide and sulfur hexafluoride in the critical region. *J Chem Thermodyn* 34:277–292. https://doi.org/10.1006/jcht.2001.0955

[89] Albright PC, Edwards TJ, Chen ZY, Sengers JV (1987) A scaled fundamental equation for the thermodynamic properties of carbon dioxide in the critical region. *J Chem Phys* 87:1717–1725. https://doi.org/10.1063/1.453238

[90] Abdulagatov IM, Polikhronidi NG, Batyrova RG (1994) Measurements of the isochoric heat capacities C_v of carbon dioxide in the critical region. *J Chem Thermodyn* 26:1031–1045. https://doi.org/10.1006/jcht.1994.1121

[91] Haase R, Tillmann W (1994) Heat capacities of one-component and two-component fluid systems in the critical region. *Z Phys Chem* 186:99–112. https://doi.org/10.1524/zpch.1994.186.Part_1.099

[92] Ernst G, Gürtner J, Beck L (1997) A c_v calorimeter of small dimension. *J Chem Thermodyn* 29:1189–1203. https://doi.org/10.1006/jcht.1997.0232

[93] Straub J (1972) The non-classical behaviour of fluids at the critical state. *Wärme Stoffübertrag* 5:56–63.
[94] Edwards TJ (1984) *Specific heat measurements near the critical point of carbon dioxide*. Ph.D. thesis. University of Western Australia, Perth, Australia.
[95] Datchi F, Weck G, Saitta AM, Raza Z, Garbarino G, Ninet S, Spaulding DK, Queyroux JA, Mezouar M (2016) Structure of liquid carbon dioxide at pressures up to 10 GPa. *Phys Rev B* 94:014201. https://doi.org/10.1103/PhysRevB.94.014201
[96] Giordano VM, Datchi F, Dewaele A (2006) Melting curve and fluid equation of state of carbon dioxide at high pressure and high temperature. *J Chem Phys* 125:054504. https://doi.org/10.1063/1.2215609
[97] Trusler JPM (2011) Equation of state for solid phase I of carbon dioxide valid for temperatures up to 800 K and pressures up to 12 GPa. *J Phys Chem Ref Data* 40:043105. https://doi.org/10.1063/1.3664915
[98] Liang Y, Zhang JT, Feng XJ, Qiu P (2023) Realization of the triple point of carbon dioxide in a transportable cell using long-stem SPRTs. *Metrologia* 60:015006. https://doi.org/10.1088/1681-7575/aca417
[99] Veltcheva R, da Silva R, Pearce JV (2024) Realization of the triple point of carbon dioxide at NPL. *AIP Conf Proc* 3230:060002. https://doi.org/10.1063/5.0234207
[100] Harvey AH (2017) On the melting curve of sulfur hexafluoride. *J Phys Chem Ref Data* 46:043102. https://doi.org/10.1063/1.5005537
[101] Ancsin J (1992) Development of cryogenic sealed cells as temperature standards: Their filling system and the purification of CO_2. *Metrologia* 29:71–78. https://doi.org/10.1088/0026-1394/29/1/009
[102] Bridgman PW (1914) Change of phase under pressure. I. The phase diagram of eleven substances with especial reference to the melting curve. *Phys Rev* 3:153–203. https://doi.org/10.1103/PhysRev.3.153
[103] Babb, Jr SE (1963) Some notes concerning Bridgman's manganin pressure scale. *High Pressure Measurement Techniques*, eds Giardini AA, Lloyd EC (Butterworths, Washington, DC), pp 115–124.
[104] Molinar GF, Bean V, Houck J, Welch B (1980) The mercury melting line up to 1200 MPa. *Metrologia* 16:21–29. https://doi.org/10.1088/0026-1394/16/1/005
[105] Michels A, Blaisse B, Hoogschagen J (1942) The melting line of carbon dioxide up to 2800 atmospheres. *Physica* 9:565–573. https://doi.org/10.1016/S0031-8914(42)80070-1
[106] Michels A, Wassenaar T, Blaisse B (1942) The melting line of mercury up to 3000 atmospheres. *Physica* 9:574–576. https://doi.org/10.1016/S0031-8914(42)80071-3
[107] Bedford RE, Bonnier G, Maas H, Pavese F (1996) Recommended values of temperature on the International Temperature Scale of 1990 for a selected set of secondary reference points. *Metrologia* 33:133–154. https://doi.org/10.1088/0026-1394/33/2/3

[108] Clusius K, Piesbergen U, Varde E (1960) Ergebnisse der Tieftemperaturforschung XXXI. Die Schmelzkurven von Kohlendioxyd und Distickstoffoxyd bis 250 atm. und ihr Volumensprung am Schmelzpunkt. *Helv Chim Acta* 43:1290–1298.
[109] Abramson EH (2017) Three-phase melting curves in the binary system of carbon dioxide and water. *J Phys: Conf Ser* 950:042019. https://doi.org/10.1088/1742-6596/950/4/042019
[110] Abramson EH (2004). Unpublished data, personal communication to A. H. Harvey in 2019, tabulated in [34].
[111] Krupskii IN, Prokhvatilov AI, Érenburg AI, Baryl'nik AS (1982) X-ray analysis of the thermal expansion of solid CO_2. *Sov J Low Temp Phys* 8:263–268.
[112] Maass O, Barnes WH (1926) Some thermal constants of solid and liquid carbon dioxide. *Proc R Soc London A* 111:224–244. https://doi.org/10.1098/rspa.1926.0065
[113] Eucken A, Hauck F (1928) Die spezifischen Wärmen c_p und c_v einiger Stoffe im festen, flüssigen und hyperkritischen Gebiet zwischen 80° und 320° abs. *Z Phys Chem* 134:161–177. https://doi.org/10.1515/zpch-1928-13413
[114] Kuenen JP, Robson WG (1902) The thermal properties of carbon dioxide and of ethane. *Phil Mag* 3:622–630. https://doi.org/10.1080/14786440209462808
[115] Giauque WF, Egan CJ (1937) Carbon dioxide. The heat capacity and vapor pressure of the solid. The heat of sublimation. Thermodynamic and spectroscopic values of the entropy. *J Chem Phys* 5:45–54. https://doi.org/10.1063/1.1749929
[116] Clusius K (1936) Atomwärmen und Schmelzwärmen von Neon, Argon, und Krypton. *Z Phys Chem* 31B:459–474. https://doi.org/10.1515/zpch-1936-3134
[117] Flubacher P, Leadbetter AJ, Morrison JA (1961) A low temperature adiabatic calorimeter for condensed substances. Thermodynamic properties of argon. *Proc Phys Soc* 78:1449–1461. https://doi.org/10.1088/0370-1328/78/6/346
[118] Egan CJ, Kemp JD (1937) Ethylene. The heat capacity from 15°K. to the boiling point. The heats of fusion and vaporization. The vapor pressure of the liquid. The entropy from thermal measurements compared with the entropy from spectroscopic data. *J Am Chem Soc* 59:1264–1268. https://doi.org/10.1021/ja01286a031
[119] Ambrose D (1956) The vapour pressures and critical temperatures of acetylene and carbon dioxide. *Trans Faraday Soc* 52:772–781. https://doi.org/10.1039/TF9565200772
[120] Fernández-Fassnacht E, Del Río F (1984) The vapour pressure of CO_2 from 194 to 243 K. *J Chem Thermodyn* 16:469–474. https://doi.org/10.1016/0021-9614(84)90204-0
[121] Barber CR (1966) The sublimation temperature of carbon dioxide. *Brit J Appl Phys* 17:391–397. https://doi.org/10.1088/0508-3443/17/3/312
[122] Baughman GL, Westhoff SP, Dincer S, Duston DD, Kidnay AJ (1974) The solid + vapor phase equilibrium and the interaction second virial coefficients for argon +, nitrogen +, methane +, and helium + neopentane I. Experimental. *J Chem Thermodyn* 6:1121–1132. https://doi.org/10.1016/0021-9614(74)90148-7
[123] Ancsin J (1978) Some properties of CO_2 (Comite Consultatif de Thermometrie, Paris), CCT/78-5.

[124] Tickner AW, Lossing FP (1951) The measurement of low vapor pressures by means of a mass spectrometer. *J Phys Chem* 55:733–740. https://doi.org/10.1021/j150488a013

[125] Bilkadi Z, Lee MW, Bigeleisen J (1975) Phase equilibrium isotope effects in molecular solids and liquids. Vapor pressures of the isotopic carbon dioxide molecules. *J Chem Phys* 62:2087–2093. https://doi.org/10.1063/1.430772

[126] Eiler JM, Kitchen N, Rahn TA (2000) Experimental constraints on the stable-isotope systematics of CO_2 ice/vapor systems and relevance to the study of Mars. *Geochim Cosmochim Acta* 64:733–746. https://doi.org/10.1016/S0016-7037(99)00327-0

[127] Bryson CE, Cazcarra V, Levenson LL (1974) Sublimation rates and vapor pressures of water, carbon dioxide, nitrous oxide, and xenon. *J Chem Eng Data* 19:107–110. https://doi.org/10.1021/je60061a021

[128] Laesecke A, Muzny CD (2017) Reference correlation for the viscosity of carbon dioxide. *J Phys Chem Ref Data* 46:013107. https://doi.org/10.1063/1.4977429

[129] Harvey AH, Lemmon EW (2025) Fluid file containing parameters for the thermophysical properties of carbon dioxide, including a new equation of state, that is readable by the NIST REFPROP computer program, National Institute of Standards and Technology. https://doi.org/10.18434/mds2-3953.

Appendix A. Uncertainty of Calculated Virial Coefficients

Estimates of the uncertainties of the values for the second virial coefficient calculated by Hellmann were already provided in [33]. They decrease from 5.4 cm^3/mol at 150 K (which is approximately 0.8 % of the total value) to 0.5 cm^3/mol at 420 K and remain at this level up to 1000 K. Above 1000 K, they increase with increasing temperature and reach 1.0 cm^3/mol at 2000 K. For the extended values of the present work down to 75 K and up to 3000 K, a probably conservative estimate is that the uncertainty increases from 0.8 % at 150 K to 5 % at 75 K and from 1.0 cm^3/mol at 2000 K to 2.0 cm^3/mol at 3000 K. All of these estimates correspond to combined expanded uncertainties with $k = 2$.

In Hellmann's work on the higher virial coefficients of CO_2 [43], uncertainty estimates were not provided for the individual virial coefficients. While the virial equation of state yields quite accurate values for the pressure as a function of density, as can be seen from the comparison with the Span–Wagner equation of state, this is partly due to an adjustment of the *ab initio* nonadditive three-body potential function. Hellmann performed this adjustment in such a manner that the calculated pressures agree well with those from the Span–Wagner EOS close to room temperature [43], which inevitably hides errors in the individual virial coefficients by forcing them to cancel out when combining all the virial coefficients into the full virial equation of state. With the adjustment, the pressure is reproduced within 0.08 % up to densities of 200 kg/m^3 at the critical temperature of 304.128 K, indicating that the individual errors of the virial coefficients cannot be severe. This conclusion is corroborated by the fact that at temperatures away from room temperature, the deviations of the calculated pressures from those obtained with the Span–Wagner EOS are still quite small at densities for which the virial equation is sufficiently converged, despite the expectation that a near-perfect cancellation of errors should no longer occur at these temperatures. It should also be noted that at temperatures above about 700 K, for the third to seventh virial coefficients the contribution from the nonadditive three-body potential is about an order of magnitude smaller than the main contribution, which is that of the pair potential. The high accuracy of the pair potential is evident from the excellent agreement of calculated values for the second virial coefficient and the dilute-gas shear viscosity with the best experimental data over a temperature range that extends from the triple-point temperature up to almost 1500 K [33].

Taking these considerations into account, a conservative estimate for the relative combined expanded uncertainty ($k = 2$) of the third virial coefficient would be 10 % from the temperature of the maximum (approximately 270 K) up to 2000 K. Below 270 K, the use of relative uncertainties is problematic because the third virial coefficient crosses zero at about 220 K. Therefore, it is assumed that the absolute uncertainty increases steadily from its value at 270 K with decreasing temperature such that at 150 K, which is the lowest temperature of the extended values of the present work, a relative uncertainty of 15 % is attained. The relative uncertainties for the higher virial coefficients should generally be somewhat larger than those for the third virial coefficient because the relative influence

of the nonadditive three-body potential increases with increasing order of the virial coefficient. At temperatures above about 700 K, where the influence of the nonadditive three-body potential is always small, it is seen as highly unlikely that the calculated values for the fourth to seventh virial coefficients are in error by more than 15 % to 25 %, respectively.